

## Wave-packet modulation in shock-containing jets

Petrônio A. S. Nogueira \* and Hamish W. A. Self 

*Department of Mechanical and Aerospace Engineering, Laboratory for Turbulence Research in Aerospace and Combustion, Monash University, Melbourne, VIC 3800, Australia*

Aaron Towne 

*Department of Mechanical Engineering, University of Michigan, 2350 Hayward Street, Ann Arbor, Michigan 48109, USA*

Daniel Edgington-Mitchell 

*Department of Mechanical and Aerospace Engineering, Laboratory for Turbulence Research in Aerospace and Combustion, Monash University, Melbourne, VIC 3800, Australia*



(Received 30 January 2022; accepted 12 July 2022; published 26 July 2022)

We propose an approach to predict the modulation of wave packets in shock-containing jets. With a modeled ideally expanded mean flow as input, an approximation of the shock-cell structure is obtained from the parabolized stability equations (PSE) at zero frequency. This solution is then used to define a new shock-containing mean flow, which is a function of the shock-cell wave number at each streamwise station. Linearization of the Navier-Stokes equations around this quasiperiodic mean flow allows us to postulate a solution based on the Floquet ansatz, and further manipulation of the equations leads to a system called the parabolized Floquet equations [PFE; Ran *et al.*, [Phys. Rev. Fluids 4, 023901 \(2019\)](#)] that bears several similarities to PSE. The modulation wave numbers are marched spatially together with the central Kelvin-Helmholtz wave number, leading to a modulated wave packet as the final solution. The limitations of PFE are highlighted, and the method is applied to two sample cases: a canonical slowly diverging jet at low supersonic Mach number and a heated overexpanded jet, for which large-eddy simulation (LES) data are available. Good agreement is observed between the wave packets predicted by PFE and the leading spectral proper orthogonal decomposition (SPOD) modes from the LES, suggesting that the method is able to capture the underlying physical mechanism associated with wave-packet modulation: the extraction of energy from the mean flow by the Kelvin-Helmholtz mode and a redistribution of energy to modulation wave numbers due to the interaction of this mode with the shock-cell structure.

DOI: [10.1103/PhysRevFluids.7.074608](https://doi.org/10.1103/PhysRevFluids.7.074608)

### I. INTRODUCTION

Understanding the relevant physical mechanisms in jet noise generation has long been a topic of great interest in the fluids community, with the goal of developing quieter engines. Starting with Mollo-Christensen [1], attention has been given to large-scale coherent structures in these flows and their connection with the far-field sound. Crow and Champagne [2] identified these structures, using smoke visualizations, which revealed trains of “puffs” with a clear amplitude modulation,

---

\*petronio.nogueira@monash.edu

comprising regions of growth, saturation, and decay. These wave-packet structures have been shown to be responsible for most of the downstream acoustic radiation in turbulent jets [3–5].

The genesis of these coherent structures was found to be in the stability characteristics of the flow: in jets and shear layers, the presence of an inflection point in the base flow leads to the appearance of an inviscid instability, namely, the Kelvin-Helmholtz (KH) mode [6,7]. This mode extracts energy from the mean flow, resulting in the highly amplified structures observed experimentally [2,8]. This clear instability mechanism inspired the development of several modeling methods to predict the key features of wave packets. While the application of locally parallel linear stability analysis resulted in only qualitative agreement with experimentally deduced KH modes [9,10], models that consider the jet development were shown to quantitatively capture the overall behavior of these waves. For instance, Crighton and Gaster [11] proposed a theoretical method based on a WKB approximation to overcome the limitations of the local analysis, obtaining the solution for a slowly varying mean flow. The parabolized stability equations (PSE), introduced by Bertolotti and Herbert [12], improved upon the WKB approach by tracking the slow downstream evolution of the shape function and wave number [13,14]. Application of PSE to predict wave-packet shapes and phase velocities was first performed by Gudmundsson and Colonius [15] for subsonic jets, which led to good agreement with modes extracted from data via spectral proper orthogonal decomposition (SPOD, Towne *et al.* [16]) at frequencies relevant to jet noise. This comparison has since been extended to higher frequencies and azimuthal wave numbers [17], ideally expanded supersonic jets [18], and jets with azimuthal nonhomogeneity [19].

Even though PSE provides a good approximation of the overall behavior of wave packets in turbulent jets at low computational cost, it also has several limitations, such as its inability to predict the wave-packet characteristics at low frequencies [15]. This problem is addressed by more advanced methods, like resolvent analysis [20]. As shown by Towne *et al.* [16], response modes predicted by resolvent analysis are closely related to the most energetic structures in the flow deduced using SPOD; in fact, if the nonlinear terms in the Navier-Stokes equations expanded about the mean flow are uncorrelated in space and time, SPOD and resolvent response modes are identical. This provides a rigorous explanation for the success of resolvent analysis in predicting coherent structures in various turbulent flows [21–27].

While these modeling approaches are well suited for the study of subsonic or ideally expanded supersonic jets, their applicability to shock-containing flows is less straightforward. As summarized in recent reviews [28,29], these flows are usually subject to a resonance phenomenon called screech, which leads to the appearance of sharp tones in the acoustic fields of imperfectly expanded jets. As shown recently by Nogueira *et al.* [30], this phenomenon is caused by an absolute instability mechanism triggered by the flow periodicity induced by the shock cells, which causes disturbances to grow in both space and time until they reach a saturated state. This absolute instability leads to unstable global modes, as shown in Beneddine *et al.* [31] (or marginally stable ones, as in Edgington-Mitchell *et al.* [32]). The high computational cost and the often intricate numerics associated with computing global modes in these flows limits their utility for wave-packet modeling. The presence of sharp discontinuities in the flow prohibits the application of PSE and other WKB-based methods as well. As shown by Bertolotti *et al.* [33], the PSE approach is beneficial only when the flow properties are slowly varying in the streamwise direction, and when the flow is only convectively unstable (in the absence of absolute instability); none of these conditions are satisfied in shock-containing jets. For that reason, most of the broadband shock-associated noise (BBSAN) prediction models are based either on first principles (as in Harper-Bourne and Fisher [34], Tam and Tanna [35], Tam [36]) or numerical simulations [37,38]. As the key mechanism of BBSAN is the interaction between instability waves and the shock-cell structure, a low-order model for predicting the equivalent shock-modulated wave packet in these jets would be useful.

Some alternatives to solve this issue have been proposed in the literature. In Ray and Lele [39], following the ideas of Tam [36], the authors build a BBSAN source term based on the interaction between a shock cell predicted from linear stability analysis, and a wave packet obtained using PSE. Even though the final source term may have the expected spectral shape (with higher energy content

at wave numbers associated with the shock-cell structure modulation), since the instability waves are computed using a shock-free mean flow, this modulation may not correspond to that observed in real flows. A similar approach was used by Wong *et al.* [40], who obtained the characteristics of the wave packet using either PSE or SPOD modes from an ideally expanded jet, and the shock-cell structure from experimental data. In both cases, the modulation of the source term of BBSAN (namely, the modulated wave packet) was obtained *a posteriori*, and the actual effects of the shocks on the KH mode could not be obtained. The periodic, locally parallel formulation developed by Nogueira *et al.* [30] is able to capture the modulation of this unstable wave under the assumption of spatial periodicity, leading to good agreement with experimental results. However, the effect of shear-layer spreading and shock-cell variation/weakening cannot be obtained using a periodic model.

In this work, the modulation of wave packets in shock-containing jets is explicitly obtained using the parabolized Floquet equations (PFE). This formulation was first developed by Ran *et al.* [41] for the study of transition mechanisms in boundary layers and is applied in the present paper to study the coherent structures supported by imperfectly expanded jets. Here the effect of the mean flow development is directly estimated, providing a low-cost method for predicting the overall characteristics of the KH wave packets in these jets.

The paper is organized as follows: in Sec. II we review the PSE formulation, which lays the foundations for the present method, and derive the PFE method for shock-containing jets. The limitations of the PFE formulation are also highlighted in Sec. II. The results provided by PFE for two sample cases are analyzed in Secs. III and IV, where comparisons with SPOD modes are also performed. The paper is concluded in Sec. V.

## II. MATHEMATICAL FORMULATION

### A. Parabolized stability equations

We start from the PSE formulation as reviewed by Herbert [14]. In summary, solutions are sought for the compressible linearized Navier-Stokes (N-S) equations, which can be written in operator form as

$$\frac{\partial \mathbf{q}}{\partial t} + \mathbf{A}\mathbf{q} + \mathbf{B}\frac{\partial \mathbf{q}}{\partial x} + \mathbf{C}\frac{\partial \mathbf{q}}{\partial r} + \mathbf{D}\frac{\partial \mathbf{q}}{\partial \theta} + \frac{1}{\text{Re}}\mathbf{E}_{r,\theta}\mathbf{q} = 0. \quad (1)$$

The state vector  $\mathbf{q} = [v \ u \ v \ w \ p]^T$  contains specific volume, streamwise, radial, and tangential velocity components and pressure, respectively.  $\text{Re}$  is the Reynolds number. All spatial coordinates are normalized by the jet diameter  $D$ , the velocity is normalized by the free-stream sound speed  $c_\infty$ , and the specific volume is normalized by its value far from the jet ( $v_\infty$ ). Following the PSE formulation, the second streamwise derivative of the disturbance vector was neglected, and the matrix  $\mathbf{E}_{r,\theta}$  is a function of the first and second radial/azimuthal derivatives of the state vector. All the operators are a function of the mean flow  $\bar{\mathbf{q}}_0$  and its spatial derivatives. To solve Eq. (1), disturbances are written in the frequency ( $\omega$ ) and azimuthal wave-number ( $m$ ) domain as

$$\mathbf{q}(x, r, \theta, t) = \tilde{\mathbf{q}}(x, r, m, \omega)e^{-i\omega t + im\theta}. \quad (2)$$

The PSE ansatz considers solutions of the form

$$\tilde{\mathbf{q}}(x, r, m, \omega) = \hat{\mathbf{q}}(x, r, m, \omega)e^{i \int^x \alpha(\xi) d\xi} = \hat{\mathbf{q}}(x, r, m, \omega)\Gamma(x) \quad (3)$$

with

$$\Gamma(x) = e^{i \int^x \alpha(\xi) d\xi}, \quad (4)$$

where both  $\hat{\mathbf{q}}(x, r, m, \omega)$  and  $\alpha(x)$  are slowly varying functions of  $x$ . This ansatz (and the Leibniz rule) allows us to write the equations as

$$-i\omega\hat{\mathbf{q}} + \mathbf{A}\hat{\mathbf{q}} + \mathbf{B}\frac{\partial \hat{\mathbf{q}}}{\partial x} + i\alpha\mathbf{B}\hat{\mathbf{q}} + \mathbf{C}\frac{\partial \hat{\mathbf{q}}}{\partial r} + im\mathbf{D}\hat{\mathbf{q}} + \frac{1}{\text{Re}}\mathbf{E}_{r,m}\hat{\mathbf{q}} = 0 \quad (5)$$

or

$$-i\omega\hat{\mathbf{q}} + \mathbf{L}\hat{\mathbf{q}} + \mathbf{B}\frac{\partial\hat{\mathbf{q}}}{\partial x} + i\alpha\mathbf{B}\hat{\mathbf{q}} = 0, \quad (6)$$

where  $\mathbf{L} = \mathbf{A} + \mathbf{C}\frac{\partial}{\partial r} + im\mathbf{D} + \frac{1}{\text{Re}}\mathbf{E}_{r,m}$ . All matrix operators are written explicitly in Appendix A for a specific volume-pressure formulation of the linearized Navier-Stokes equations [42].

In order to remove the ambiguity between the slowly varying variables  $\hat{\mathbf{q}}$  and  $\alpha$ , the normalization condition

$$\int_0^{r_{\max}} \hat{\mathbf{q}} \frac{\partial\hat{\mathbf{q}}^*}{\partial x} r dr = 0 \quad (7)$$

is imposed in the method (see Herbert [13] for further details), where the asterisk superscript represents the complex conjugate. By discretizing the streamwise derivatives using first-order implicit Euler differences, (6) and (7) can be written as [15]

$$[\Delta x(-i\omega\mathbf{I} + \mathbf{L} + i\alpha\mathbf{B}) + \mathbf{B}]_{j+1}\hat{\mathbf{q}}_{j+1} = \mathbf{B}_{j+1}\hat{\mathbf{q}}_j \quad (8)$$

and

$$\alpha_{j+1}^{(n+1)} = \alpha_{j+1}^{(n)} - \frac{i}{\Delta x} \frac{\int_0^\infty (\hat{\mathbf{q}}_{j+1}^{(n)})^* (\hat{\mathbf{q}}_{j+1}^{(n)} - \hat{\mathbf{q}}_j) r dr}{\int_0^\infty |\hat{\mathbf{q}}_{j+1}^{(n)}|^2 r dr}. \quad (9)$$

Thus, given an initial solution  $\hat{\mathbf{q}}_{x=x_0}$ ,  $\alpha_{x=x_0}$  obtained close to the nozzle, the PSE system can be marched in the downstream direction from station  $x_j$  to  $x_{j+1}$  by solving the resulting discretized linear system shown in (8). The wave number  $\alpha$  is then updated at each station using (8) and (9) until convergence. This leads to the final solution of the PSE for each frequency and azimuthal wave number.

### B. Parabolized Floquet equations

The modulation of wave packets caused by the shock-cell structure will be modeled using the parabolized Floquet equations (PFE), first introduced by Ran *et al.* [41] for the study of interactions between different modes in boundary layer transition. To this point, the PSE analysis has considered an ideally expanded supersonic mean flow. A first-order approximation [43] of an equivalent shock-containing flow can be obtained from the zero-frequency PSE solution as

$$\bar{\mathbf{q}} = \bar{\mathbf{q}}_0 + \bar{\mathbf{q}}_s \Gamma_s + \bar{\mathbf{q}}_s^* \Gamma_s^*, \quad (10)$$

where  $\bar{\mathbf{q}}_s$  and  $\Gamma_s$  are related to the zero-frequency/zero-azimuthal wave-number PSE solution by

$$\bar{\mathbf{q}}_s(x, r) = \hat{\mathbf{q}}(x, r, \omega = m = 0) e^{-\int^x \alpha_i(\xi) d\xi}, \quad (11)$$

$$\Gamma_s(x) = e^{i \int^x \alpha_s(\xi) d\xi}, \quad (12)$$

where  $\alpha_i$  is the imaginary part of the wave number  $\alpha$  obtained from the zero-frequency PSE and  $\alpha_s$  is the real part. Considering that the shock cells decay slowly (around the same rate of the mean flow spreading),  $\bar{\mathbf{q}}_s$  is also a slowly varying function of  $x$ . The separation in (11) and (12) is done such that the term  $\Gamma_s$  is associated with the streamwise variation of the shock-cell wave number only. Also, since  $\alpha_s$  is a real function,  $\Gamma_s^* = e^{-i \int^x \alpha_s(\xi) d\xi}$ .

Since the shock-containing mean flow has a component associated with the shock-cell structure (with nonzero streamwise wave numbers), we may propose a slightly different solution for (1). Using the Floquet anzats [44], a solution that considers a central wave number and the modulation by the shock cells can be written as

$$\tilde{\mathbf{q}}(x, r) = \sum_{j=-N}^N \hat{\mathbf{q}}_j(x, r) \Gamma(x) \Gamma_s^j(x), \quad (13)$$

where  $N$  is the number of harmonics considered in the analysis (the frequency/azimuthal wave-number dependence of the solution is implied). In contrast to PSE, our objective is to find not only  $\Gamma(x)$  and  $\hat{\mathbf{q}}_0(x, r)$ , but also the slowly varying parts associated with the modulation wave numbers  $\alpha \pm j\alpha_s$  (which are due to the product  $\Gamma(x)\Gamma_s'(x)$ ). The outputs of the formulation are the slowly varying parts of the central  $\hat{\mathbf{q}}_0$  and modulated  $\hat{\mathbf{q}}_{\pm j}$  wave numbers and the streamwise development of the central wave number  $\alpha(x)$ . Thus, the solution will account for the downstream-traveling Kelvin-Helmholtz mode and the modulation components related to the shock-cell wave number (which is allowed to vary slowly in the streamwise direction). By inserting (13) into the linearized N-S equations, a set of equations for each modulation component can be written (the detailed process for  $N = 1$  is shown in Appendix A), which allows us to write the equivalent PFE system as

$$-i\omega\hat{\mathbf{q}} + \mathbf{L}_t\hat{\mathbf{q}} + \mathbf{B}_t\frac{\partial\hat{\mathbf{q}}}{\partial x} + i\alpha\mathbf{B}_t\hat{\mathbf{q}} + i\alpha_s\mathbf{B}_{st}\hat{\mathbf{q}} = 0, \quad (14)$$

where the vector  $\hat{\mathbf{q}} = [\hat{\mathbf{q}}_{-N} \cdots \hat{\mathbf{q}}_0 \cdots \hat{\mathbf{q}}_N]^T$  comprises all the modulation components. The explicit form of the matrix operators is shown in Appendix A.

The above system has exactly the same form as (6) and will be solved in the same fashion. The spatial marching method is implemented as in PSE, with the wave number  $\alpha$  being updated in a similar manner by imposing

$$\int_0^{r_{\max}} \hat{\mathbf{q}}_0 \frac{\partial\hat{\mathbf{q}}_0^*}{\partial x} r dr = 0. \quad (15)$$

Equation (15) can be viewed as a first approximation of (7) and assumes the amplitude of the modulation components to be small. Overall, PSE and PFE share several technical similarities, including the fact that both methods are based on a separation of scales of the flow. Thus, the resulting wave packets are quasimodal, with slowly varying phase velocities and local growth rates [41,45]. These assumptions may hinder the application of the method in cases where nonmodal/multimodal behavior is expected (especially if more than one unstable mode is present in the flow, such as in coaxial jets). It may also find issues in cases where there are sudden variations in the flow. However, both PSE and PFE are expected to work fairly well in problems where a single KH instability is the dominant mechanism [17,46]. The connection of both methods to locally parallel linear stability analysis and some of their underlying limitations are highlighted in the next sections.

### C. The initial step of PFE

Both PFE and PSE (which can be regarded as a special case of PFE for  $N = 0$ ) requires an initial perturbation to be marched downstream using implicit Euler differences. This solution is obtained by solving the eigenvalue problem defined by

$$-i\omega\hat{\mathbf{q}} + \mathbf{L}_t\hat{\mathbf{q}} + i\alpha\mathbf{B}_t\hat{\mathbf{q}} + i\alpha_s\mathbf{B}_{st}\hat{\mathbf{q}} = 0 \quad (16)$$

or, defining  $\mathbf{F} = -(-i\omega\mathbf{I} + \mathbf{L}_t + i\alpha_s\mathbf{B}_{st})$ ,

$$\mathbf{F}\hat{\mathbf{q}} = i\alpha\mathbf{B}_t\hat{\mathbf{q}}, \quad (17)$$

which is obtained by neglecting the streamwise derivatives in (14), and assuming the mean flow to be either spatially periodic (if  $N > 0$ ) or locally parallel ( $N = 0$ ). If  $N > 0$ , (17) is equivalent to the spatially periodic linear stability analysis (SPLSA) formulation described in Nogueira *et al.* [30], now written in terms of each modulation component of the resulting eigenmode, and truncated to the number of harmonics considered in the problem. The main differences between locally parallel linear stability analysis (LSA) and SPLSA spectra are shown schematically in Fig. 1. Similar to the description of Towne *et al.* [45], Fig. 1 highlights the two acoustic branches (associated with waves traveling downstream and upstream), the upstream-traveling stable guided jet (GJ) mode, the downstream-traveling unstable KH mode, and their complex conjugates. In the PSE/LSA case, the KH mode is readily identified in the spectrum and used as initial solution in the spatial march. This is

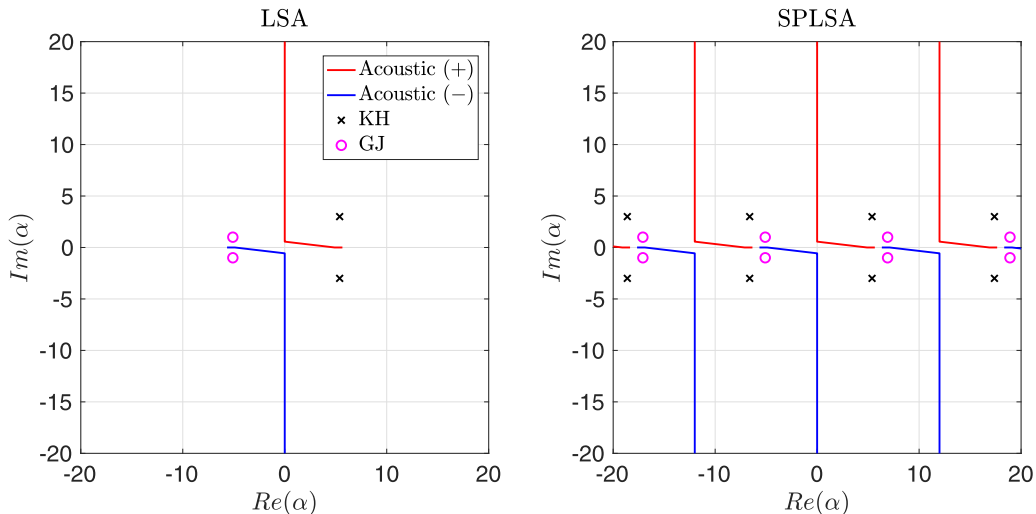


FIG. 1. Sketch highlighting the differences between LSA and SPLSA spectra. Both upstream- and downstream-traveling acoustic branches are shown (blue and red lines), together with the discrete Kelvin-Helmholtz ( $\times$ ) and guided jet ( $\circ$ ) modes.

not as straightforward in the PFE/SPLSA case. As detailed in Nogueira *et al.* [30], if  $\alpha_p$  is a complex eigenvalue of the problem and  $\alpha_s$  is the spatial periodicity wave number, eigenvalues following  $\alpha_p \pm n\alpha_s$  (with integer  $n$ ) will also be solutions, leading to an  $\alpha_s$ -periodic spectrum. That periodic behavior leads to the appearance of upstream modes close to the KH mode in the spectrum, allowing for interactions between these modes if the shock-cell amplitude is nonzero; in fact, it is exactly this kind of interaction that underpins the appearance of screech tones in the flow [30,47]. Since PFE is applicable to convectively unstable modes due to its inability to account for upstream-traveling waves intrinsic to absolute instability [48], this mode interaction is undesirable and may lead to instabilities in the numerical method. This phenomenon is further detailed in the next section.

One should also note that the resulting eigenfunctions from SPLSA will also follow the same spatial periodicity as the mean flow, and may have energy at modulation wave numbers  $\text{Re}[\alpha_p \pm n\alpha_s]$ . This is also in contrast with LSA, which results in modes with a single wave number. This distinction between LSA and SPLSA is also extended to PSE and PFE: while PSE computes modes with a single wave number (and small variations around it), PFE modes are composed by a central slowly varying streamwise wave number and several modulation wave numbers associated with the oscillatory part of the shock-cell structure. Thus, while LSA/PSE may be suitable for the study of waves in ideally expanded flows, their periodic counterparts (SPLSA/PFE) form an alternative set of tools to be applied in shock-containing jets.

#### D. Step-size restriction for PFE

As shown by Li and Malik [49] and further explored by Towne *et al.* [45], the presence of stable upstream-traveling waves in the spectrum of PSE may lead to an instability in the spatial march. A stability analysis of the PSE march leads to the minimum step-size restriction (or the minimum step one can choose and still avoid instability)

$$\Delta x > \Delta x_0 = \max \left( -2 \frac{\text{Im}[\alpha_u - \alpha_0]}{|\alpha_u - \alpha_0|} \right), \quad (18)$$

where  $\alpha_0$  is the wave number of the mode being marched downstream,  $\text{Im}$  stands for imaginary part, and the maximum is taken over all upstream-traveling modes  $\alpha_u$ . Usually, the  $\alpha_u$  mode that

TABLE I. Minimum step size of PFE as function of number of harmonics considered and the ideally expanded Mach number for  $St = 0.7$ .

$M_j$	$\Delta x_0 (N = 0)$	$\Delta x_0 (N = 1)$	$\Delta x_0 (N = 2)$
1.086	0.1592	0.1972	0.1972
1.2	0.1592	1.0335	1.0335
1.7	0.1592	0.3591	1.4010

maximizes the expression is part of the upstream-traveling free-stream acoustic branch, which for zero free-stream velocity can be approximated as

$$\alpha_u = -\omega\sqrt{1 - z^2}, \quad (19)$$

where  $z \in [0, \infty)$  is equivalent to a transverse wave number. Using this expression for  $\alpha_u$  and working with the inequality (18) leads to the classic PSE step-size requirement

$$\Delta x_0 = \frac{1}{|\text{Re}[\alpha_0]|}. \quad (20)$$

As in PSE, PFE also has requirements regarding the stability of the spatial march. Similar to the spatially periodic analysis [30], the spectrum from PFE is composed of the main PSE spectrum (with wave numbers  $\alpha_{PSE}$ ) and modes related to the inclusion of the harmonics (wave numbers  $\alpha_{PSE} \pm n\alpha_s$ ), as shown schematically in Fig. 1. This leads to the appearance of upstream acoustic modes in the spectrum with wave numbers

$$\alpha_u = -\omega\sqrt{1 - z^2} \pm n\alpha_s. \quad (21)$$

Thus, the requirement of (18) can now be reworked to consider the repetition of the spectrum, which leads to a minimum step size of

$$\Delta x_0 = \max \left( \frac{1}{|\text{Re}[\alpha_0] \pm n\alpha_s|} \right), \quad (22)$$

with the maximum taken for  $-N \leq n \leq N$ , with  $N$  the number of harmonics considered in the problem.

While the PFE formulation was derived for an incompressible boundary layer in Ran *et al.* [41], the authors did not derive the minimum step size of the formulation in that previous work; this is the first time that it is presented. The equation above shows that the minimum step size of PFE can be larger than the one from PSE, depending on the shock-cell wave number. This means that the issues from the PSE method are aggravated in PFE, which sets some limits for its applicability. It is expected that PFE would work as well as PSE for low supersonic Mach numbers in underexpanded jets issuing from purely convergent nozzles (which have high  $\alpha_s$ ). As the Mach number is increased, the shock-cell wave number decreases, leading to more strict step-size requirements. For example, Table I shows the minimum step size of PFE assuming the march of a Kelvin-Helmholtz mode with phase velocity  $0.7U_j$  ( $U_j$  is the ideally expanded jet velocity) for  $N = 0, 1$  and  $2$  and normalized frequency  $St = 2\pi\omega D/U_j = 0.7$ . It is clear that, while  $\Delta x_0$  does not change much with  $N$  for low supersonic Mach numbers, it increases substantially for higher  $M_j$ . Table I shows how the minimum step size can be strongly affected by the presence of the acoustic branches, depending on the position of the mode in the spectrum and the shock-cell wave number. For some cases, the step-size restriction renders the method impractical, as will be exemplified in the next sections. In order to mitigate the issue, the stabilization procedure described in Andersson *et al.* [50] was also implemented. This relaxes the step-size restriction by replacing the dissipation from the large implicit steps with a damping term whose magnitude is proportional to the minimum step size. One should note that, even though this method addresses one of the issues of the spatial march, it still

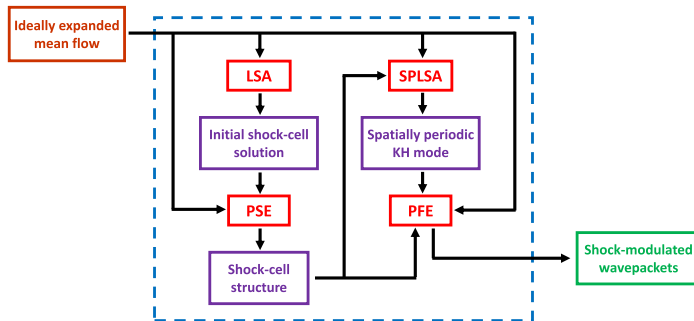


FIG. 2. Flowchart depicting the different processes undertaken to obtain shock-modulated wave packets using PFE.

relies on the knowledge of a minimum step size and is not expected to solve all the problems with the PSE/PFE formulations [45].

The present lower bounds were derived assuming that the destabilizing upstream modes belong to the continuous acoustic branch. However, as will be shown in the next sections, other upstream modes may arise in the spectrum, further restricting the minimum step size. As discrete upstream-traveling modes arise at specific bands of frequencies in high-subsonic and supersonic jets [51,52], additional care must be taken to avoid these modes in the spatial march.

### III. MODEL PROBLEM: UNDEREXPANDED $M_j = 1.086$ jet

With the method outlined, we now proceed to the analysis of the results generated by PFE. The analysis is performed for two sample cases: an  $M_j = 1.086$  underexpanded jet issuing from a converging nozzle and a heated  $M_j = 1.35$  overexpanded jet issuing from a converging-diverging nozzle (design Mach number  $M_d = 1.5$ ). In both cases, the mean temperature profile is obtained using a Crocco-Busemann approximation. The radial coordinate is discretized using Chebyshev polynomials [53] with the radial mapping proposed by Lesshafft and Huerre [54]; the number of radial collocation points was  $N_r = 200$  for all the cases studied herein. Boundary conditions were implemented as in Lesshafft and Huerre [54], and the maximum radial position of the domain was chosen as  $r_{\max}/D = 50$ .

The overall process to obtain shock-modulated wave packets using PFE is shown in Fig. 2. Spatial linear stability analysis is applied at the initial station of the flow to estimate the initial solution to be marched using PSE. As described in Tam *et al.* [43] and Choi and Lele [55], the spatial eigenspectrum of the linearized equations for  $\omega = m = 0$  possess a family of ductlike eigenmodes close to the real axis. These eigenvalues have a real part similar to the solution of Pack [56], and the shapes of the eigenfunctions are also comparable to this vortex-sheet-like model (especially if the shear layer is thin, and the Reynolds number is high). These eigenvalues are associated with the different shock-cell modes. For this case, the PSE spatial march captures both the variation in spacing of the shock cells and their amplitude decay. Still, preliminary results suggest that this variation in spacing may be better captured by using an eddy-viscosity model and by the addition of several shock-cell modes [55]. As modes predicted using PSE have a free amplitude, the scaling of the shock-cell structure must be defined *a posteriori*. Here we take advantage of the fact that the pressure mismatch at the nozzle plane in imperfectly expanded jets is only a function of the ideally expanded Mach number and the nozzle design Mach number. Thus, the amplitude and phase of these modes can be obtained directly by imposing the theoretically predicted pressure mismatch at the nozzle plane, as in Tam *et al.* [43]. Choosing the first shock-cell mode as the initial solution for PSE, the mode is marched from the nozzle ( $x = 0$ ) until the desired position downstream. In this

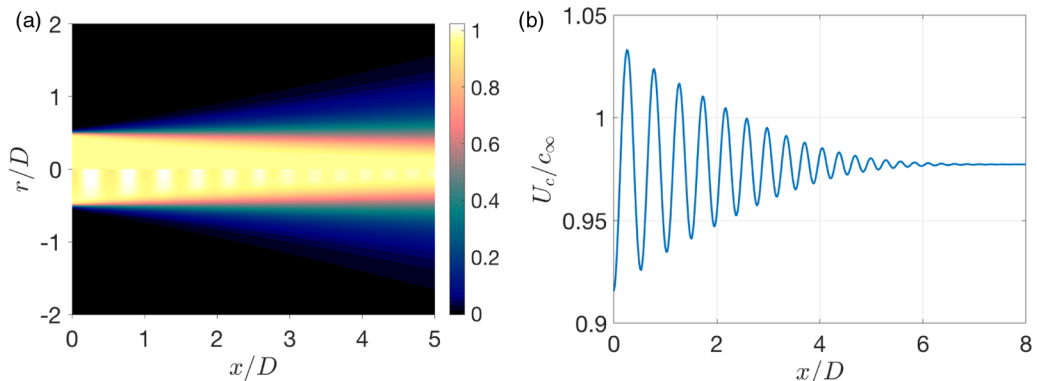


FIG. 3. Development of the mean streamwise velocity with (bottom) and without (top) the shock-cell structure (a) and mean velocity at the centerline (b) for the shock-containing case. The shock-containing solution is obtained by superposing the PSE solution with the ideally expanded mean flow.

work, a spatial step of  $\Delta x = 1/k_{\text{shock}}$  is used for the shock-cell computation, where  $k_{\text{shock}}$  is the first approximation of the shock-cell wave number obtained by Pack [56]. This step is required to obtain the slowly varying functions that represent the shock-cell structure, which will be used in PFE. In the PFE step, solutions are marched for  $N = 0$  and 4, where  $N$  is the number of harmonics considered in the problem ( $N = 0$  is equivalent to PSE); increasing the number of harmonics beyond  $N = 4$  does not lead to significant changes in the resulting modes. The SPLSA eigenvalue problem is solved using the Arnoldi method as implemented in the Matlab function `eigs`, which is used as input for PFE. After the spatial march is finished, the resulting slowly varying functions ( $\hat{\mathbf{q}}$  and  $\alpha$ ) are interpolated onto a finer equispaced mesh for plotting purposes. The final modulated wave-packet shape is obtained at this step. The step sizes chosen for PSE and PFE are given by (20) and (22), with  $\alpha_0 = k_{\text{shock}}$  (the shock-cell wave number from Pack [56]) and  $\alpha_0 = 2\pi St/0.7$  (which considers a KH mode with phase velocity  $0.7U_j$ ), respectively. In all cases, KH wave packets were computed in the  $\text{Re} \rightarrow \infty$  limit. Since all mean flows are obtained using analytical models, the mean radial velocity was neglected in all cases studied herein [45,57].

We start with the low-supersonic underexpanded case. As in Crighton and Gaster [11], the shock-free mean streamwise velocity is modeled as

$$U(x, r) = \frac{M}{2} \left\{ 1 + \tanh \left[ \frac{a_1}{a_2 x + a_3} \left( \frac{0.5}{r} - \frac{r}{0.5} \right) \right] \right\}, \quad (23)$$

where  $M = U_j/c_\infty$  is the acoustic Mach number, and  $a_1 = 10$ ,  $a_2 = 2.5$ ,  $a_3 = 1$ . Using this equivalent ideally expanded mean flow, the shock-cell structure is computed using PSE, as described in Sec. II A, setting  $\text{Re} = 200$ . This Reynolds number may appear very low; however, this value functions as the equivalent turbulent Reynolds number for the zero-frequency equation, which is subject to high-amplitude Reynolds stresses. These terms will effectively damp the shock cells in the streamwise direction, affecting its variation in spacing. This value is also close the one used by Tam *et al.* [43] in a similar computation. The mean streamwise velocity with and without shock cells is shown in Fig. 3(a). For this low-supersonic case, the shock cells are very weak, and most of their effect on the mean flow is in the potential core of the jet; the shear layer is not significantly modified in this case. As expected, the development of the mean flow and the action of viscosity lead to a decrease in the shock-cell amplitude further downstream, which is also highlighted in Fig. 3(b), where the mean streamwise velocity at the centerline is shown. The growth of the shear layer shifts the sonic line towards the centerline, shortening the distance between shock reflection points, which leads to an increase in the shock-cell wave number. These effects were already observed in previous works [43,55] and are highlighted here for clarity.

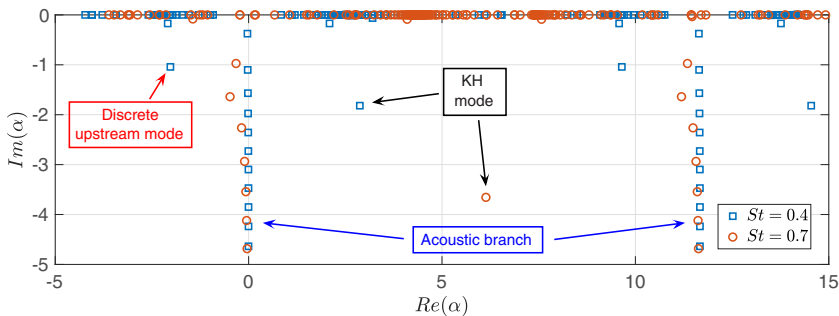


FIG. 4. Eigenspectra of the truncated spatially periodic linear stability analysis for  $St = 0.4$  and  $0.7$ , with  $N = 4$ . Only 500 eigenvalues are shown for each frequency.

Following the PFE method, the flow is now linearized around the resulting mean flow obtained from the ideally expanded mean flow and the PSE solution for the shock cells. In this example case, only axisymmetric disturbances ( $m = 0$ ) will be analyzed. As mentioned earlier, the initial step of PFE requires a SPLSA solution truncated to the number of harmonics ( $N$ ) considered in the formulation, where the wave number associated with the periodicity is defined by the wave number of the shock-cell structure at the initial streamwise station. Figure 4 shows sample eigenspectra for the present flow at  $St = 0.4$  and  $0.7$ , where similar features to those described in Nogueira *et al.* [30] are observed. First, the same modes that appear in the locally parallel case are also evident here; however, these modes now appear several times in the spectrum, with repeated modes offset from each other by  $\alpha_s$ . This is exemplified by the evanescent acoustic branch: for both frequencies, this branch arises at  $Re(\alpha) = 0$  and  $Re(\alpha) = \alpha_s = 11.6$ , with the equivalent occurring for the discrete upstream mode and the KH mode. As mentioned in Sec. II D, this repetition of the spectrum leads to the stable/evanescent upstream modes being interpreted by the spatial march as unstable downstream-traveling modes. Frequencies where the KH mode is close to the guided jet mode are also expected to be close to the screech frequency, as shown in Nogueira *et al.* [30]. Due to the presence of both downstream- and upstream-traveling waves in frequencies where absolute instability occurs, the PFE method is not appropriate to analyze the resulting flow structures involved in this phenomenon. Thus, these frequencies will be avoided in the present analysis.

Figure 5 shows the shapes of the KH modes considered as the initial solution of PFE for  $St = 0.4$  and  $0.7$ . Overall, the shapes of the solutions are similar to the ones presented in Nogueira *et al.* [30], with the effects of the modulation observed mainly around the centerline. Comparing Figs. 5(a) and 5(b), it seems that the lower frequency is more affected by modulation components associated with higher harmonics; this is confirmed in Fig. 5(c), where the streamwise velocity fluctuations at the centerline are shown. It is also clear that the modulation wave numbers for both frequencies are exactly the same, which is a consequence of the ansatz used in the formulation. Figure 5 also suggests that, even though there is a modulation for both frequencies, this modulation is fairly weak at the initial step.

The solution shown in Fig. 5 is marched downstream using the PFE method, which allows us to obtain the modulated wave packets supported by the shock-containing mean flow at each frequency. Figures 6 and 7 show, respectively, streamwise velocity and pressure fields obtained using PFE for  $St = 0.4$  and  $0.7$ , where both the real part (top) and absolute value (bottom) are shown to highlight the oscillatory behavior and the modulation of the wave packets. In these figures, the first row (a, b) depicts the total field obtained from PFE, and the subsequent rows show isolated components  $\hat{\mathbf{q}}_0$  (c, d),  $\hat{\mathbf{q}}_{+1}$  (e, f), and  $\hat{\mathbf{q}}_{-1}$  (g, h). Overall, the structures are very similar to previous PSE results (see Sinha *et al.* [18], for instance): the initial KH solution grows exponentially in the early stations of the jet, then it saturates and decays as the shear layer thickens further downstream. While the oscillatory behavior and the growth/decay of the solution are similar to KH wave packets in ideally

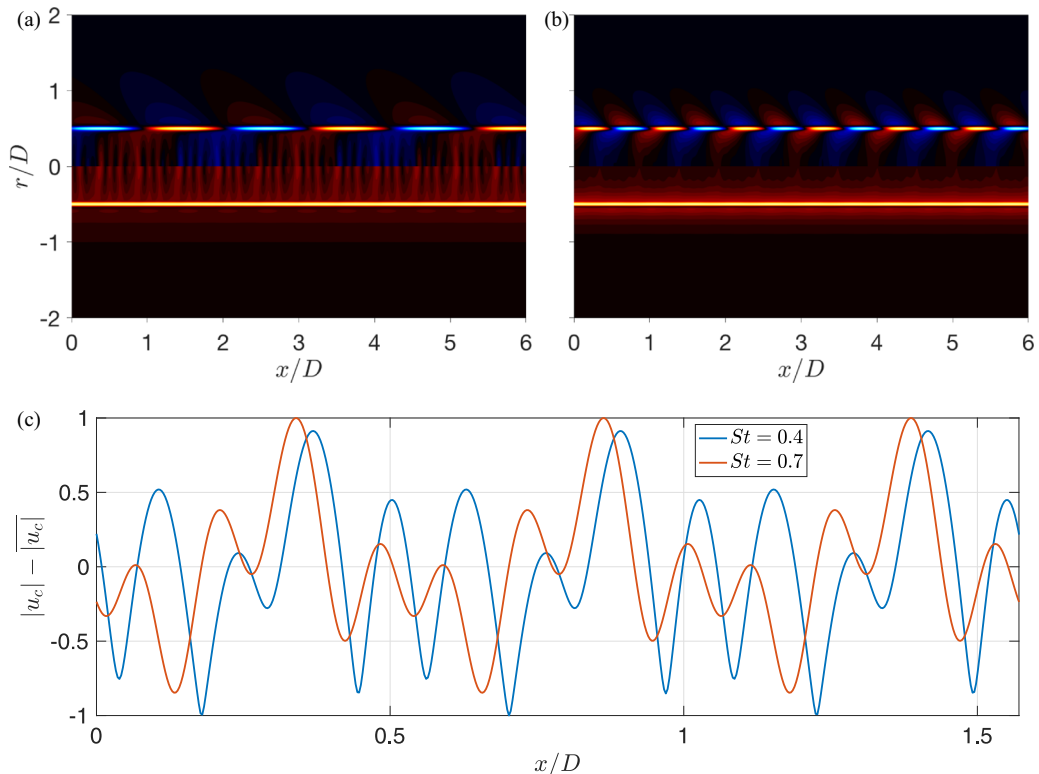


FIG. 5. Spatial reconstruction of the streamwise velocity fluctuations associated with the initial perturbation (KH) eigenfunctions for  $St = 0.4$  (a) and  $0.7$  (b); both real part (top) and absolute value (bottom) are shown. Absolute value of the streamwise velocity fluctuations at the centerline subtracted from its streamwise mean (c). In all cases the imaginary part of  $\alpha$  was neglected to highlight the effect of the modulation.

expanded jets [21], some features of the solutions are unique to PFE, and these are better seen in the absolute value of the reconstructed fields in Figs. 6(a) and 6(b) and 7(a) and 7(b). In all cases, the amplitude envelope of the wave packet has an oscillatory behavior, especially close to the centerline (where the shock-cell structure has maximum amplitude). These oscillations are associated with the modulation wave numbers included in the spatial march which, for this case, leads to the high-wave number structures observed in the total field (due to the number of harmonics considered in the analysis).

The wave-packet modulation can be more clearly evaluated by analyzing the structure of each modulation component, which can be isolated from the total field in (13). The zeroth, first positive and first negative components of the modulation are shown in Figs. 6(c)–6(h) and 7(c)–7(h). As the modulation of the wave packet comes from the modulation wave numbers, the zeroth component is directly comparable to an equivalent PSE solution computed around a shock-free mean flow, possessing the same qualitative features. Comparing with the total field, it is also clear that this component is the most energetic one, defining the shape of the final solution. Overall, the shapes of the positive modulation components are very similar for both frequencies, with a single peak close to the centerline and almost zero amplitude in the subsonic region of the jet. This behavior is consistent with the hypothesis that the effect of the shock cell on the KH mode should be more evident close to the peaks of the shocks in the simplified model. These components also follow the growth/decay behavior of the KH mode, which agrees with the theory developed by Tam and Tanna [35]; as the KH mode is the only structure capable of extracting energy from the mean flow, the energy growth

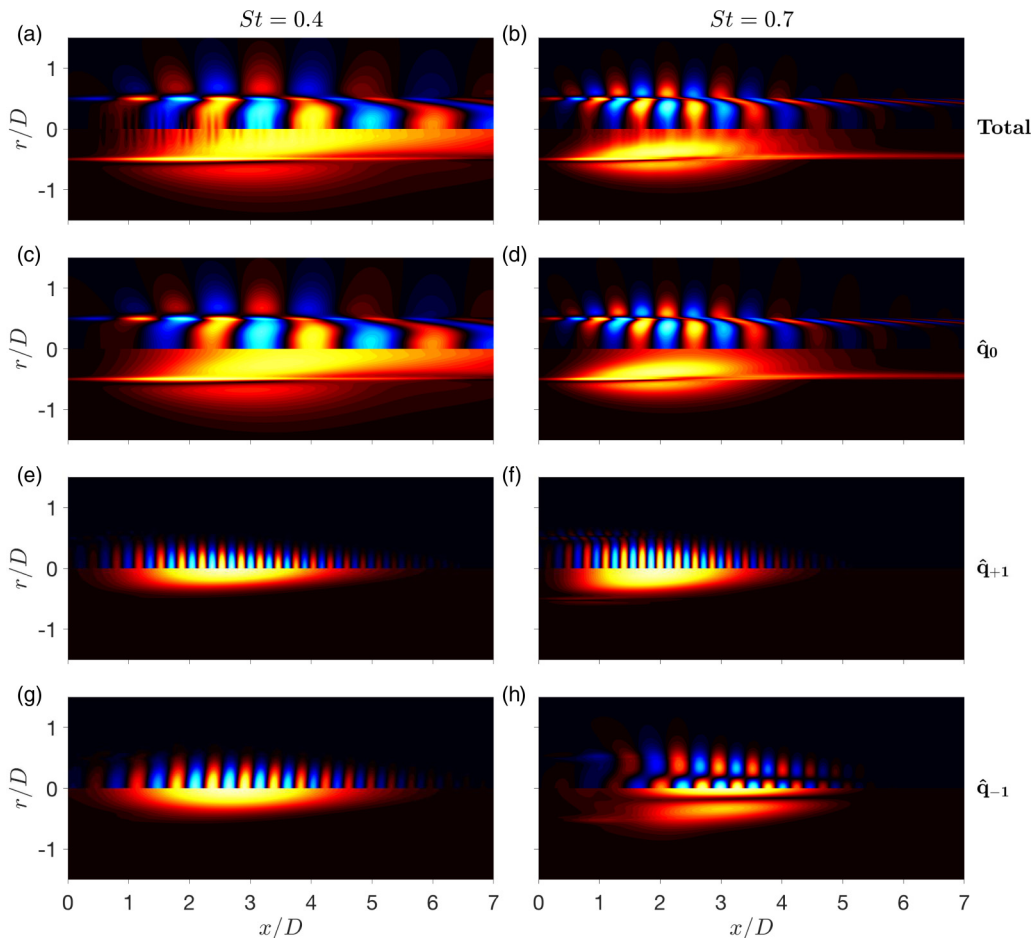


FIG. 6. Streamwise velocity fields predicted by PFE for  $St = 0.4$  (a, c, e, g) and  $0.7$  (b, d, f, h). Both real part (top) and absolute value (bottom) are shown. Fields are reconstructed in space using all modulation components and  $N = 4$  in (a) and (b). Components  $\hat{q}_0$  (c, d),  $\hat{q}_{+1}$  (e, f), and  $\hat{q}_{-1}$  (g, h) are also shown.

of the modulation wave numbers must be chained to the growth of the unstable mode. As expected, the positive part of the modulation is associated with higher wave numbers. The spatial support of the negative component of the modulation is similar to the positive one for  $St = 0.4$ . However, as the wave number of this structure is given by the difference between the wave number of the KH mode and the local wave number of the shocks, this modulation leads to structures with larger wavelength when compared to the positive modulation. Interestingly, the negative part of the modulation for  $St = 0.7$  [Figs. 6(h) and 7(h)] differs from its low frequency counterpart, having a double-peak structure. Considering that the second radial order guided jet mode is propagative at this frequency and that the resulting shape of this modulation component is very similar to the cited mode [58], it is possible that the presence of the neutral upstream mode in the spectrum is affecting the spatial march, leading to the appearance of this mode for negative wave numbers, instead of the modulation of the KH mode. This is also supported by the apparent switch from single- to double-peak structure at the early stations of the jet, also seen in Fig. 6(h).

This sample case mimics the conditions of the  $M_j = 1.086$  underexpanded jet analyzed in Edgington-Mitchell *et al.* [32]. Due to experimental limitations, no time-resolved data could be obtained in the cited work (as is often the case in shock-containing jets), hindering the identification

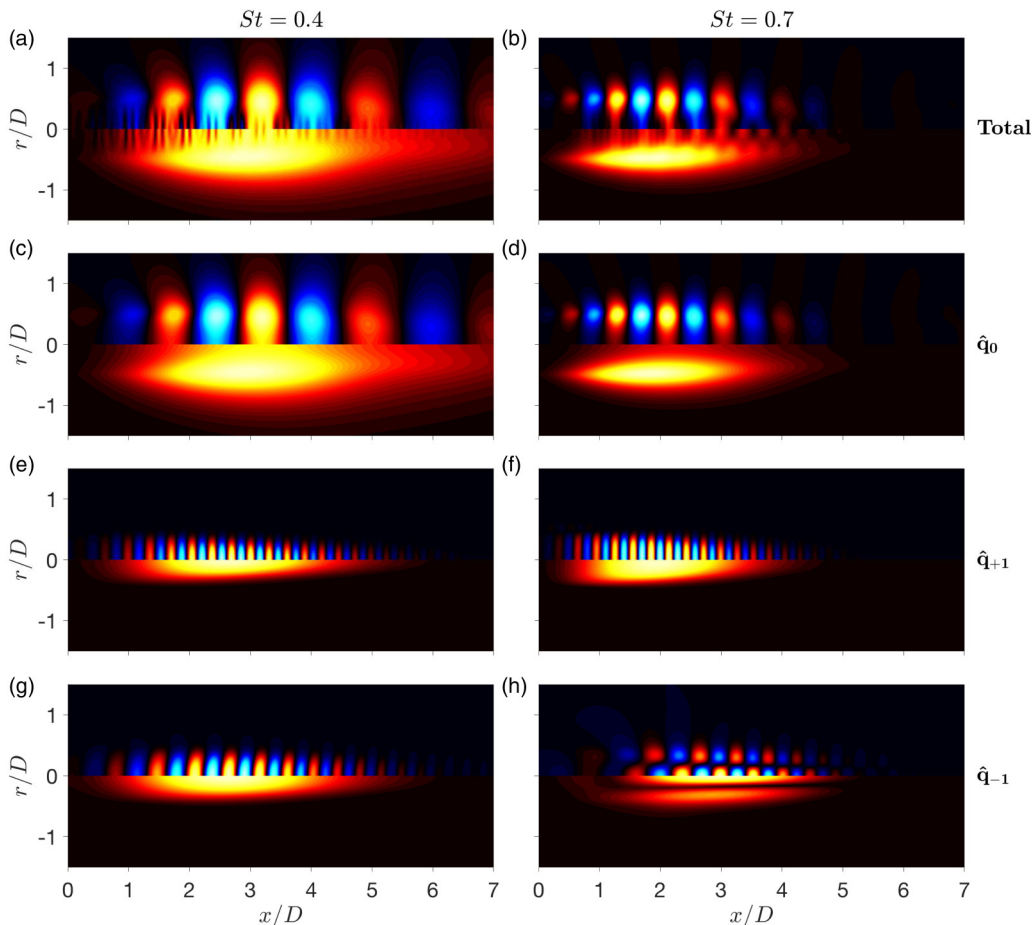


FIG. 7. Pressure fields predicted by PFE for  $St = 0.4$  (a, c, e, g) and  $0.7$  (b, d, f, h). Both real part (top) and absolute value (bottom) are shown. Fields are reconstructed in space using all modulation components and  $N = 4$  in (a) and (b). Components  $\hat{q}_0$  (c, d),  $\hat{q}_{+1}$  (e, f), and  $\hat{q}_{-1}$  (g, h) are also shown.

of wave packets at off-resonance frequencies. In this previous case, proper orthogonal decomposition (POD) was applied to particle-image velocimetry data of the screeching jet, which allowed for the extraction of the most energetic coherent structure associated with the resonance process. This resonance process leads to the appearance of strongly amplified upstream waves, resulting in flow structures whose main features, such as the strong modulation around the shear layer, are captured by the absolute instability analysis [30]. As mentioned earlier, the presence of both upstream- and downstream-traveling waves in the flow at the resonance condition prohibits the application of PFE [33], and the resulting modulated wave packet close to the screech frequency can only be analyzed as if there were no screech. With that in mind, the structure of the wave packet for  $St = 0.7$  also possesses a similar modulation around the centerline, suggesting that some of the features of the modulated wave packet are preserved in the resonance condition. As mentioned earlier, the structures of the main modulation components [Figs. 6(f) and 6(h)] are also very similar to the wavelike structures highlighted in Edgington-Mitchell *et al.* [32] for  $St = 0.7$ . This may be due to the presence of both downstream- and upstream-traveling neutral modes in the spatial march, or simply due to the difficulty in separating the structure of the modulation from the different waves supported by the flow.

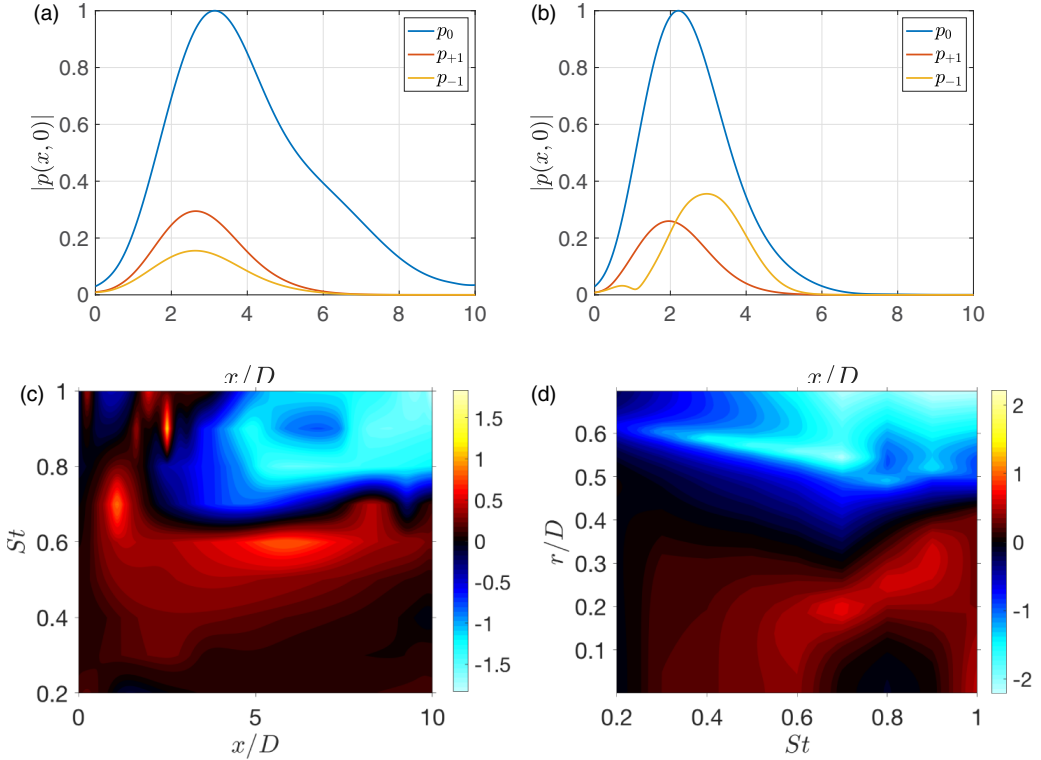


FIG. 8. Amplitude of the different components for  $St = 0.4$  (a) and  $0.7$  (b) for  $r/D = 0$ . Ratio between positive and negative components of the modulation  $[\log(|p_{+1}|/|p_{-1}|)]$  for a range of frequencies and  $r/D = 0$  (c) and  $x/D = 2$  (d) with  $\Delta St = 0.1$ .

As mentioned in Sec. IID (and exemplified in Fig. 4), the PFE method is subject to the same issues as PSE, where any stable upstream-traveling mode in the spectrum is considered as an unstable downstream-traveling mode, which may lead to a spurious growth of these modes. This becomes even more serious with the repetition of the spectrum in the PFE method: the spatial step must be chosen to damp the evanescent acoustic branch at  $\text{Re}(\alpha) = 0$  at low frequencies, and also its replica at  $\text{Re}(\alpha) = \alpha_s$  at higher frequencies. Still, other modes may arise in the analysis that could impact the spatial march. In particular, the neutral upstream acoustic branch may lead to the inclusion of an upstream wave in the march, as shown in the previous section; since this wave is not evanescent, this does not lead to the growth of spurious waves, but may lead to nonphysical results due to the parabolization of the equations. In theory, the correct behavior of the upstream waves (including their respective modulation) could only be obtained using the equations parabolized in the opposite direction, which would march the desired mode from a given position downstream until the nozzle. This issue with upstream waves becomes worse for frequencies at which the guided jet mode becomes stable [51,52,58], which usually occurs at frequencies higher than the screech frequency. In those cases, the PFE method must be further stabilized to avoid considering this mode in the march, which also affects the resulting modulated wave packet.

This is further explored in Fig. 8. In Figs. 8(a) and 8(b), the magnitude of the central solution and the different modulation components at the centerline are shown for  $St = 0.4$  and  $0.7$ . For  $St = 0.4$ , the amplitude of the positive modulation  $|p_{+1}|$  is higher than the negative one  $|p_{-1}|$  at all streamwise stations. That is not the case for  $St = 0.7$ : even though  $|p_{+1}|$  is dominant very close to the nozzle,  $|p_{-1}|$  increases substantially after reaching low amplitudes; at this point, the source of

this change in shape of the negative modulation is unclear. It is possible that the presence of the neutral guided jet mode at this frequency may influence the shape of the final solution, while the spatial march is kept stable due to the stabilization procedure [50]. Figure 8(c) shows the logarithm of the relative magnitude of positive and negative modulation [ $\log(|p_{+1}|/|p_{-1}|)$ ] at the centerline for several frequencies and streamwise stations. Even though these wave components decay quite strongly further downstream, they never reach zero amplitudes in the domain studied herein. In Fig. 8(c), red and blue regions should be interpreted as dominance of the positive and negative modulation components, respectively. This result shows the dominance of the positive modulation up to  $St = 0.6$ , supporting the hypothesis that the neutral guided jet mode (which is propagative for  $St > 0.67$  at the initial station  $x/D = 0$ ) starts to influence the spatial march at higher frequencies. For the present case, this wave becomes stable at the initial streamwise station for  $St = 0.8$ ; thus, for that frequency, the damping factor of Andersson *et al.* [50] had to be further increased to avoid a dominance of the stable guided jet mode. Overall, the radial structure of the negative modulation component is still very similar to the one for  $St = 0.7$ , but its streamwise behavior is less clear. Due to the underlying limitations of PFE, there is no guarantee that the results at these high frequencies will correspond to the physics of the problem. A similar trend is observed in Fig. 8(d), where the radial behavior of the modulation ratio is shown for several frequencies: for low  $St$ ,  $|p_{+1}|$  dominates over  $|p_{-1}|$  until positions close to the shear layer, suggesting that positive modulation decays faster in the radial direction. For  $St \geq 0.7$ , a red peak which could be associated with the phase change of the neutral upstream wave is observed around  $r/D = 0.2$ . Again, it is possible that the negative modulation for these high frequency cases is contaminated by stable upstream waves, which may change its radial shape. However, a confirmation of the source of this change in spatial support of the negative part of the modulation can only be performed if the upstream modes are completely removed from the spatial march, which can be attained by using a one-way Navier-Stokes formulation [59].

In summary, these results suggest that PFE is able to capture some of the main features associated with wave-packet modulation, providing a predictive model to be applied to shock-containing jets. However, one should be cautious when applying the method for high frequencies, especially when the shock-cell wave number is small (as is usually the case in highly underexpanded jets). With that in mind, we can now proceed to a validation case, where the PFE results will be compared to SPOD modes of an overexpanded jet.

#### IV. VALIDATION: OVEREXPANDED $M_j = 1.35$ jet

Next, we explore a large-eddy simulation database similar to the one described in Brès *et al.* [60] generated using the compressible flow solver ‘‘Charles,’’ developed by Cascade Technologies. It comprises an overexpanded jet issuing from a round converging-diverging nozzle with design Mach number  $M_d = 1.5$ , operating at an ideally expanded jet Mach number  $M_j = 1.35$  and nozzle temperature ratio  $NTR = 2.53$ . The main differences compared to this previous simulation are the Reynolds number ( $Re_j = 760\,000$ ), the presence of wall modeling inside the nozzle, and a near-wall adaptive mesh refinement (see Brès *et al.* [61]). The total simulation time was  $\Delta t c_\infty/D = 500$ , and fields were saved at a sampling frequency of  $fD/c_\infty = 10$ , resulting in 5000 snapshots. The data are interpolated onto a structured cylindrical grid with dimensions  $N_x \times N_r \times N_\theta = 698 \times 136 \times 128$ , ranging  $0 \leq x/D \leq 30$ ,  $0 \leq r/D \leq 6$ , and an azimuthal decomposition is performed using  $n_{fft,\theta} = 128$ . Further details about the LES simulation can be found in Brès *et al.* [60].

As in several previous works [15,17,18,21,62], PFE results will be compared to the most energetic structures extracted from the flow using spectral proper orthogonal decomposition (SPOD). Following Towne *et al.* [16], these structures are obtained by solving the integral eigenvalue problem

$$\int_{\Omega} \mathbf{S}(x, x', r, r', m, \omega) \boldsymbol{\psi}(x', r', m, \omega) r' dr' dx' = \sigma(m, \omega) \boldsymbol{\psi}(x, r, m, \omega), \quad (24)$$

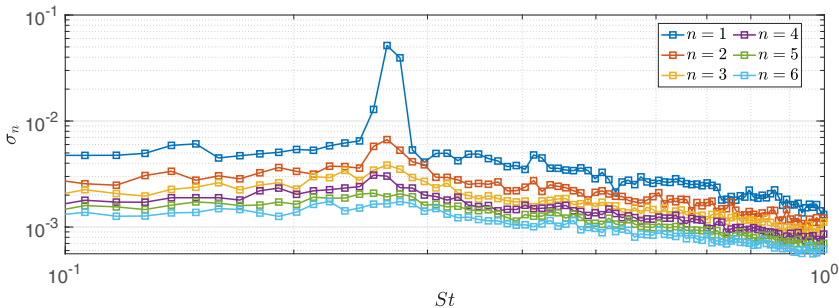


FIG. 9. First six spectral proper orthogonal decomposition eigenvalues as function of Strouhal number.

where  $\mathbf{S}$  is the two-point cross-spectral density (CSD) tensor of flow fluctuations (which can be built using any of the available variables), and  $\Omega$  is the computational domain. Solution of (24) leads to real, positive eigenvalues  $\sigma$  (which are associated with the relative energy of each mode), and orthogonal eigenfunctions  $\boldsymbol{\psi}$ . Thus, the most energetic structures of the jet are associated with the first eigenvalue  $\sigma_1$ , and its respective eigenfunction  $\boldsymbol{\psi}_1$  for each frequency. The CSD tensor is computed for a reduced domain ( $0 \leq x/D \leq 10$ ,  $0 \leq r/D \leq 2$ ) using  $n_{fft} = 512$  and 75% overlap, leading to 36 blocks in the Welch method, and a discretization in frequency of  $\Delta St \approx 0.01$ . In the present case, we will focus on helical ( $m = 1$ ) pressure disturbances.

The SPOD eigenspectrum is shown in Fig. 9. Unlike subsonic and ideally expanded supersonic jets [21], the spectrum displays a sharp peak around  $St = 0.26$ , associated with the screech tone. This tone is a direct consequence of an absolute instability mechanism induced by the shock-cell periodicity, where flow disturbances grow in both downstream and upstream directions [30]. Since PFE can only obtain downstream-traveling waves, the flow structure associated with this tone will not be further analyzed herein.

Following the same methodology described in Sec. II, we define a realistic flow model as an input for both PSE and PFE. In this case, the equivalent ideally expanded streamwise velocity is based on the expression proposed by Sandham and Salgado [63], which is given by

$$U(x, r) = \frac{M}{2} \left[ \tanh \left( \frac{r + a(x)}{\delta(x)} \right) - \tanh \left( \frac{r - a(x)}{\delta(x)} \right) \right], \quad (25)$$

where

$$a(x) = D_j [0.59 + 0.09 \tanh(\sqrt{x/\kappa} - 2.9)] \quad (26)$$

and

$$\delta(x) = \frac{7 + 70(x/\kappa) + 0.15(x/\kappa)^4}{1000 + (x/\kappa)^3}. \quad (27)$$

The coefficients in (27) were chosen to provide a similar development of the sonic line when compared to the LES (as zero-frequency PSE results are very sensitive to that parameter, especially concerning the variation in shock-cell spacing further downstream). The value  $\kappa = 1.475$  was obtained by means of a least-squares-based fit of the mean streamwise velocity at the centerline. The ideally expanded diameter  $D_j$  (normalized by  $D$ ) is obtained as in Tam *et al.* [43]. As in the previous case, the temperature and density profiles were obtained using a Crocco-Busemann approximation and the ideal gas law. In the absence of a model for the shock-free mean radial velocity, this component was also neglected, and the Reynolds number for the PSE march was defined as  $Re = 175$  (which is considered to be equivalent to a turbulent Reynolds number for the mean flow equation).

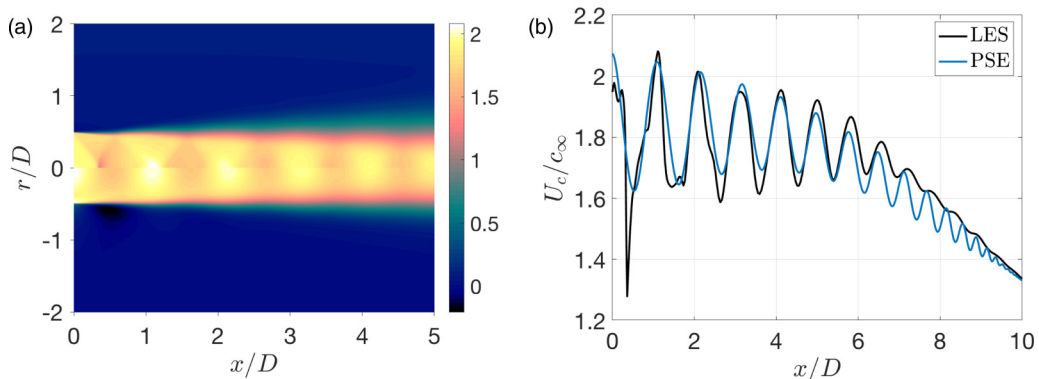


FIG. 10. Mean streamwise velocity computed from the LES (top) and by a superposition of a modeled ideally expanded flow and the shock-cell structure predicted using zero-frequency PSE (bottom) (a). Comparison between the mean streamwise velocity at the centerline from LES and the present method (b).

The resulting mean streamwise velocity predicted from zero-frequency PSE is compared to the LES results in Fig. 10. As shown in Fig. 10(a), the overall behavior of the mean flow is well captured by the model, especially concerning the shock cells. The shear layer from the LES is thicker at some streamwise stations, but the sonic lines for the two cases are comparable, which led to favorable agreement for the shock cells further downstream. The PSE is unable to account for the Mach reflection near the centerline of the first shock cell, leading to an overprediction in the streamwise velocity. However, both the amplitude and spacing of subsequent shock cells is predicted well, in line with the results of Harper-Bourne and Fisher [34]. This is confirmed in Fig. 10(b), where the mean streamwise velocities at the centerline are compared. PSE seems to capture the general behavior of the shock cell, including its amplitude, until about  $x/D = 6$ ; after that, this structure is strongly damped in the LES, an effect that is not captured by the model. Considering the differences in the mean flow characteristics, the absence of a streamwise varying turbulent viscosity, and that only a single shock-cell mode is included in the analysis, these results can be considered as a good first approximation of the shock-cell train in this turbulent jet. Better agreement with the simulation data (including the sharper changes associated with the shocks) can be obtained if more modes are included in the analysis [43,55]. For the expansion conditions of the present jet, Pack [56] predicts a shock-cell wave number of  $k_{\text{shock}}D = 5.3$ , which is significantly smaller than the case studied in the previous section. Thus, it is expected that PFE may struggle to produce good predictions at mid-high frequencies, since the range of frequencies where the KH mode is far from any upstream mode in the PFE eigenspectrum is rather small. Furthermore, since only a single shock-cell mode is included in the mean flow computation, the current PFE results will only consider the modulation associated with that specific mode. Higher order shock-cell modes, which are known to play an effect on BBSAN [40] are not included, even though they may be present in the SPOD modes.

The amplitude scaling of the PFE results is not as straightforward as the zero-frequency PSE. It is also more involved compared to the scaling for shock-free mean flows; the smoothness of the solution for ideally expanded jets allows one to obtain their amplitude using experimental/simulation data at a given point of the flow (see Gudmundsson and Colonius [15], Cavalieri *et al.* [62], for instance). In contrast, the final PFE solutions are not smooth (even though each modulation component is); they are composed by several modulation wave numbers, which leads to final modes that have fast variations in the streamwise direction after spatial reconstruction. For that reason, a scaling using a single point in the flow may hinder the comparison between PFE and SPOD, as any small mismatch in the phase of the modulation components at a given upstream position may lead to large differences in the amplitude of the final mode at positions further downstream. Here both SPOD and PFE modes are scaled to have the same maximum amplitude. Even though this scaling

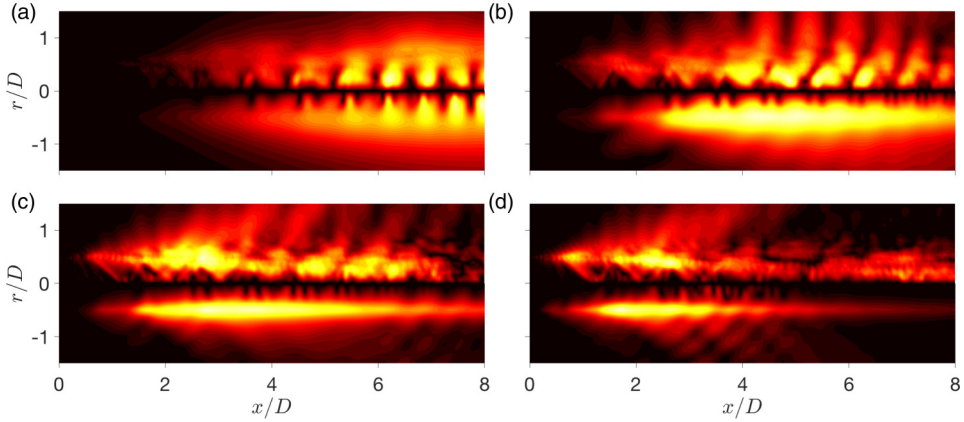


FIG. 11. Comparison between leading SPOD modes from LES (top) and the flow structure predicted by PFE (bottom) using  $N = 4$  and several frequencies. Absolute value of the modes are shown for  $St = 0.19$  (a),  $0.4$  (b),  $0.74$  (c), and  $0.91$  (d).

is not as robust as the one used for shock-free jets, it is sufficient for a comparison of wave-packet shapes.

A comparison between the first SPOD mode from LES and the wave packets predicted using PFE is shown in Fig. 11 (absolute value) and Fig. 12 (real part), for four sample frequencies ( $St = 0.19$ ,  $0.4$ ,  $0.74$  and  $0.91$ , chosen as to avoid the cases where the KH mode is close to upstream waves in the spectrum). For this case, given the step-size restrictions and the repetition of the spectrum, the lowest frequency ( $St = 0.19$ ) is expected to provide the most favourable comparison, as no upstream waves strongly affect the spatial march. For this frequency, the PFE captures the overall behavior of the amplitude envelope, which extends until the end of the domain. While the modes do not seem to capture the modulation particularly well at the early stations of the jet, it performs very well closer to the peak of the KH mode, especially near the centerline (where the shocks are strongest). The three other frequencies are higher than the screech tone, and will potentially be more affected by

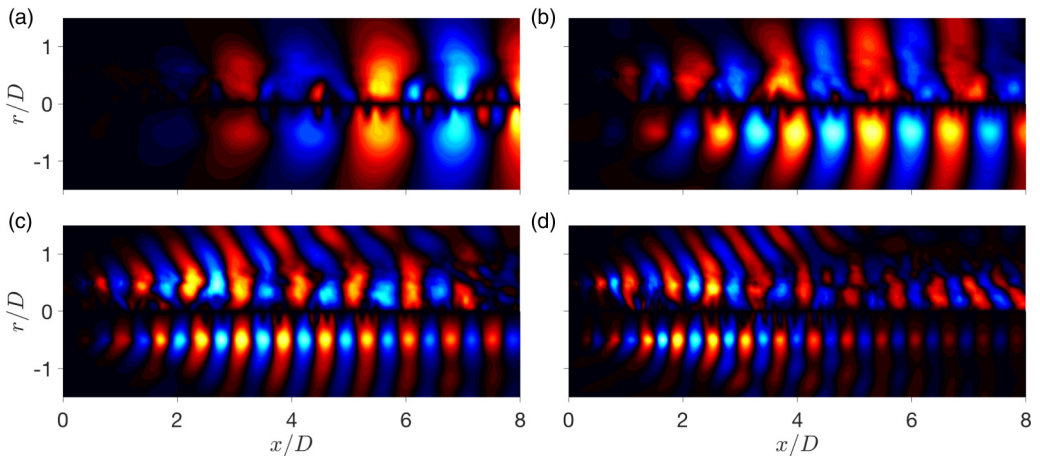


FIG. 12. Comparison between leading SPOD modes from LES (top) and the flow structure predicted by PFE (bottom) using  $N = 4$  and several frequencies. Real part of the modes are shown for  $St = 0.19$  (a),  $0.4$  (b),  $0.74$  (c), and  $0.91$  (d).

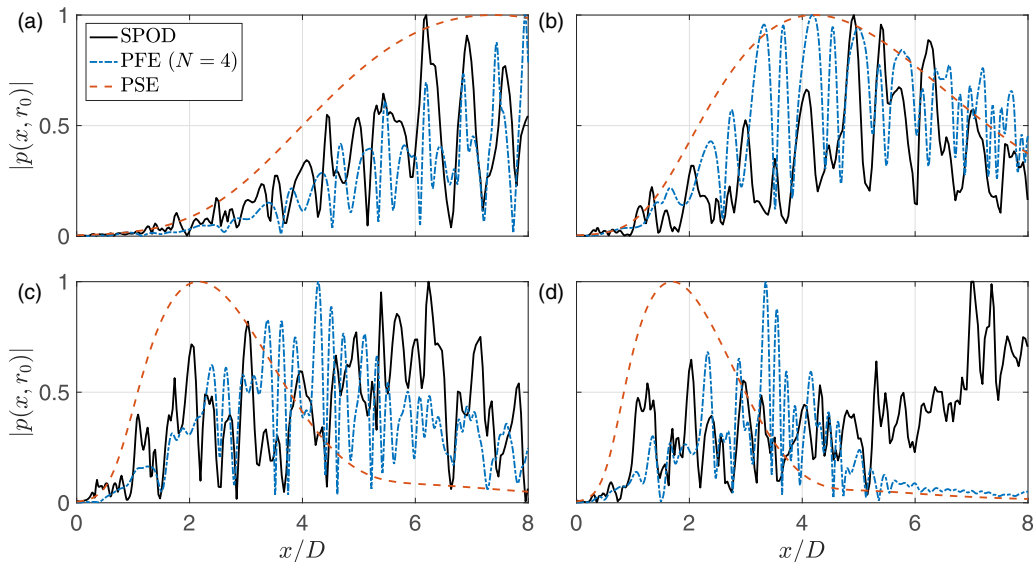


FIG. 13. Absolute value of leading SPOD modes from LES compared to PFE ( $N = 4$ ) and PSE results for several frequencies. Magnitude of the modes extracted at  $r/D = 0.1$  for  $St = 0.19$  (a),  $0.4$  (b),  $0.74$  (c), and  $0.91$  (d). All curves are normalized by their maximum.

upstream modes. Nevertheless, the overall envelope length is very similar for all cases, and PFE also manages to capture some key features of the modulation, including the oscillations close to the centerline. For  $St = 0.4$ , the SPOD mode has a clear standing wave pattern, suggesting the presence of strong upstream waves in the flow; obviously, PFE is not able to capture these waves, and the modulation around the shear layer is underpredicted as a result. A similar behavior is observed for  $St = 0.74$ , where a modulation due to upstream acoustic waves is also observed in the outer part of the shear layer. For  $St = 0.91$ , multiple acoustic beams are identified in both SPOD and PFE (better seen in Fig. 12), with the latter being modulated by the presence of vertical waves in the flow (again, due to the proximity of the KH mode to the evanescent acoustic branch). These acoustic waves are damped in the PFE results due to the stabilization methods intrinsic to the formulation, as explained in Towne *et al.* [45]. As in previous cases [17], a second structure is observed further downstream for the highest frequency in the SPOD, which is not captured by the present model.

The real part of both SPOD and model results are shown in Fig. 12, where the wavelengths of the structures can be compared. As mentioned in Sinha *et al.* [18], PSE can predict moderately different wavelengths due to its normalization condition, and this is also shown to occur for PFE (which relies on the same condition). However, PFE still manages to predict the dominant wave numbers of these structures, especially for the lowest frequency. The presence of higher wave number structures at  $St = 0.19$  is also clear in Fig. 12 for both PFE and SPOD, which is an effect of the strong modulation for this case. The radial structures of both the model and the SPOD modes are also in good agreement (similar to PSE) for all frequencies. Acoustic waves are more clearly observed in the near field of the jet for  $St = 0.74$  and  $0.91$ , but these are poorly predicted by the PFE, as highlighted earlier. Thus, while the present analysis may be able to predict the modulation characteristics of the hydrodynamic field, the method may not be suitable for the analysis of the near acoustic field. Due to the absence of upstream modes close to the KH mode, PSE may actually perform better in the direct prediction of the downstream noise generated by Mach wave radiation. Some sample results of PSE using the shock-containing mean flow from the LES as input are shown in Appendix B.

Figure 11 suggests that, in most cases, the PFE manages to reasonably approximate the modulation of wave packets closer to the centerline. This is confirmed in Fig. 13, where the absolute

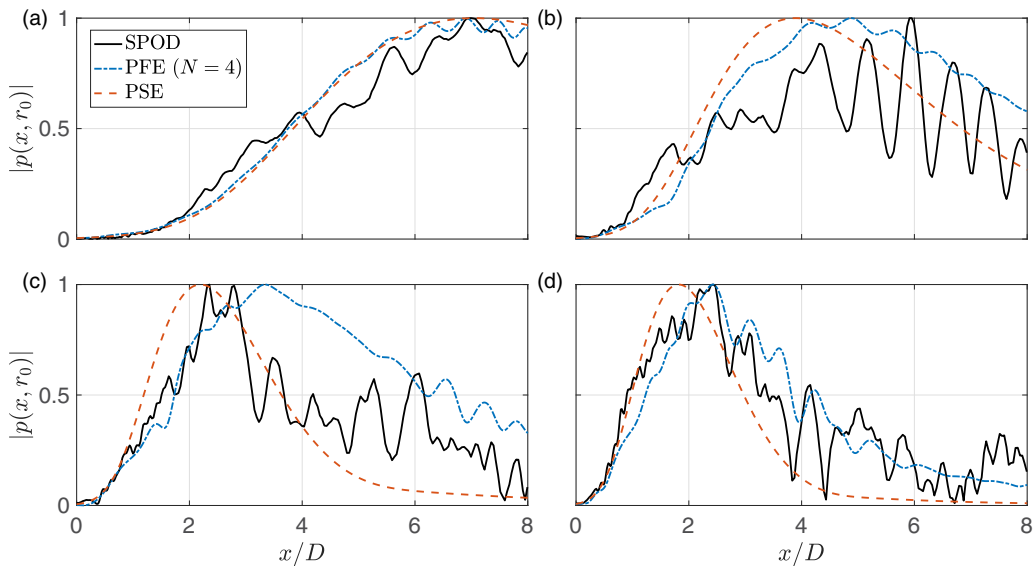


FIG. 14. Absolute value of leading SPOD modes from LES compared to PFE ( $N = 4$ ) and PSE results for several frequencies. Magnitude of the modes extracted at  $r/D = 0.7$  for  $St = 0.19$  (a),  $0.4$  (b),  $0.74$  (c), and  $0.91$  (d). All curves are normalized by their maximum.

value of the modes predicted from PFE are compared to SPOD modes at  $r/D = 0.1$ . Wave-packet shapes predicted by PSE computations using the same ideally expanded mean flow (without shocks) are also plotted for reference. The positions of the peaks in the modulated wave packets are in fair agreement with the SPOD in most cases. For lower frequencies, these peaks are either in the same position (as in most streamwise stations for  $St = 0.19$ ) or shifted slightly downstream. This shift may be due to the difficulty of PSE (and PFE) in predicting the exact wave numbers of the structures; since the modulation is obtained in the model by constructive/destructive interference of the wavelike structures related to the different harmonics, a slight shift in the wave numbers of these structures will lead to a mismatch in the position of the peaks in the reconstructed wave packet. The prediction of these peaks is slightly improved for higher frequencies, as shown in Figs. 11(c) and 11(d), where the bulk of the modulation seems to be captured. Keeping in mind that only the modulation associated with the first shock-cell mode is represented in PFE, an overall qualitative agreement is observed between model and SPOD. It is also clear that PFE outperforms PSE in the prediction of the envelope of these coherent structures, especially for higher frequencies. For those cases, PSE consistently predicts wave packets with a faster downstream decay. As PFE models the energy flux between different wave numbers due to consideration of quasiperiodicity, it is possible that this interaction induces a slower decay of the KH mode for those high frequencies. Considering the good agreement between PSE and SPOD modes for ideally expanded jets shown in Sinha *et al.* [18], this also suggests that the presence of a shock-cell structure is the cause for the increase of the wave-packet length for this case, and that PFE is able to capture such a mechanism.

Since the model struggles to predict the near acoustic field of shock-containing jets, the agreement for higher radial positions deteriorates, especially for higher frequencies (where strong Mach-wave radiation is observed). This is shown in Fig. 14, where  $r/D = 0.7$  is chosen. At this position, the model still seems to capture the overall growth of the wave packet in a similar fashion to PSE for low frequencies, with a reduced modulation effect. In particular, the standing wave pattern is absent from the model for  $St = 0.4$  for reasons already highlighted. The modulation is more strongly captured at the higher frequencies, where peaks in the envelope of the structure are

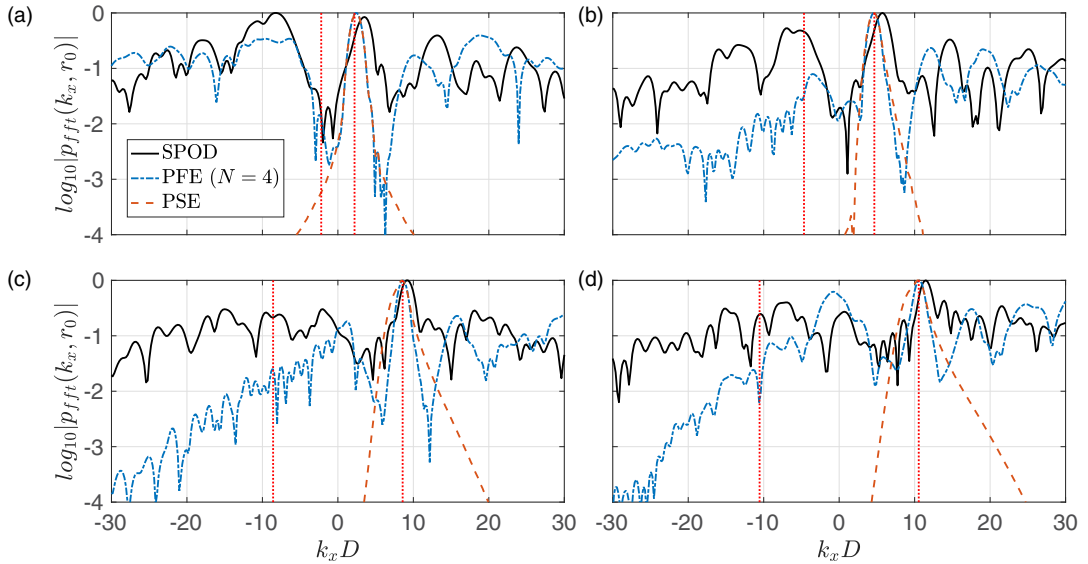


FIG. 15. Logarithm of the absolute value of leading SPOD modes from LES compared to PFE ( $N = 4$ ) and PSE results for several frequencies in the wave-number domain. Magnitude of the modes extracted at  $r/D = 0.1$  for  $St = 0.19$  (a),  $0.4$  (b),  $0.74$  (c), and  $0.91$  (d). Dotted lines indicate the acoustic wave numbers. All curves are normalized by their maximum.

comparable to SPOD modes. A very good agreement for  $St = 0.91$  is observed at this position, despite the inability of the model to correctly capture acoustic waves.

To evaluate the ability of PFE to capture the spectral energy content of the resulting wave packets, a comparison with SPOD modes in the wave-number domain is shown in Fig. 15. Since results were generated for  $x/D \leq 10$ , the spatial Fourier transforms may be contaminated by domain truncation; a Hann window was applied to both SPOD and PFE modes to minimise these effects. For all frequencies, PSE performs reasonably well in capturing the peak wave number of wave packets in this flow, but other energetic wave numbers observed in the SPOD modes are suppressed due to the absence of a shock-cell structure and the PSE regularization [45]. The energy of the PSE results at negative wave numbers (responsible for upstream noise radiation) is several orders of magnitude lower than the peak for low  $St$ , and almost negligible for higher frequencies. While not perfectly aligned, the PFE wave-number spectra bear several similarities with the SPOD spectra, including the presence of peaks at similar wave numbers. The absence of upstream waves in the PFE leads to a less energetic spectrum for negative wave numbers, especially for higher frequencies. Still, both PFE and SPOD have significant energy content at propagative wave numbers (indicated by the dotted lines in Fig. 15), suggesting that propagation of PFE wave packets to the far-field using an acoustic analogy [64] may lead to the correct acoustic directivity [4] and that wave-packet-shock modulation is the dominant source of BBSAN.

Flow structures coming from SPOD have no restriction about which kind of waves will be present in the flow; in fact, it is expected that strong upstream acoustic waves are present in this flow for mid-high frequencies (where BBSAN is active), such as the ones analyzed herein. These waves are the source of the modulation of the resulting modes at  $r/D > 1$ , which is absent in the PFE solution; this is one of the causes of the disparity observed between PFE and SPOD. This is also highlighted in Fig. 15, where it is clear that PFE struggles to capture the negative part of the spatial spectrum due to its inability to correctly represent upstream-traveling waves in the flow. There is no practical way of separating the contribution of upstream waves and the modulation associated with negative wave numbers in SPOD, complicating fair comparison of wave packets

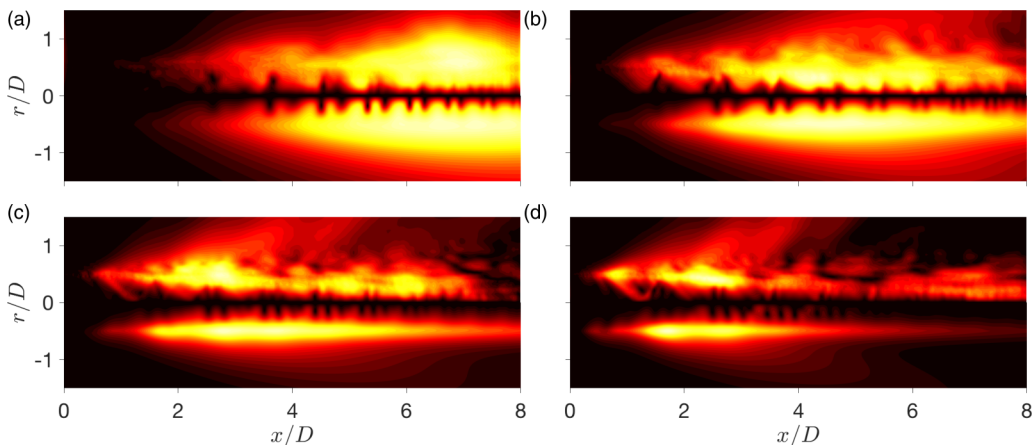


FIG. 16. Comparison between leading SPOD modes from LES (top) and the flow structure predicted by PFE (bottom) using  $N = 4$  and several frequencies. Absolute value of the modes are shown for  $St = 0.19$  (a),  $0.4$  (b),  $0.74$  (c), and  $0.91$  (d). Only positive wave numbers are allowed in the SPOD, and the PFE reconstruction is performed using nonnegative components.

from PFE and SPOD. One way to approximate that separation is to neglect the negative part of the spectrum altogether, and evaluate if the positive part of the spectrum is well represented in the physical domain. To analyze that, SPOD modes are next filtered to consider only positive wave numbers (using a rectangular bandpass filter), and PFE modes were reconstructed using only their nonnegative components (in this case,  $\hat{q}_0$  and  $\hat{q}_{+n}$ , with  $n = 1, 2, 3, 4$ ). One should keep in mind that even though the negative wave numbers are not considered in this comparison directly, their effect on the central and modulation wave numbers will still be present; for instance,  $\hat{q}_0$  is still affected by  $\hat{q}_{-1}$  in the solution, as all components are marched together. This filtering process will only minimise the errors related to the poor prediction of the negative part of the modulation in the reconstructed mode at higher frequencies. Figures 16 and 17 show the comparison between

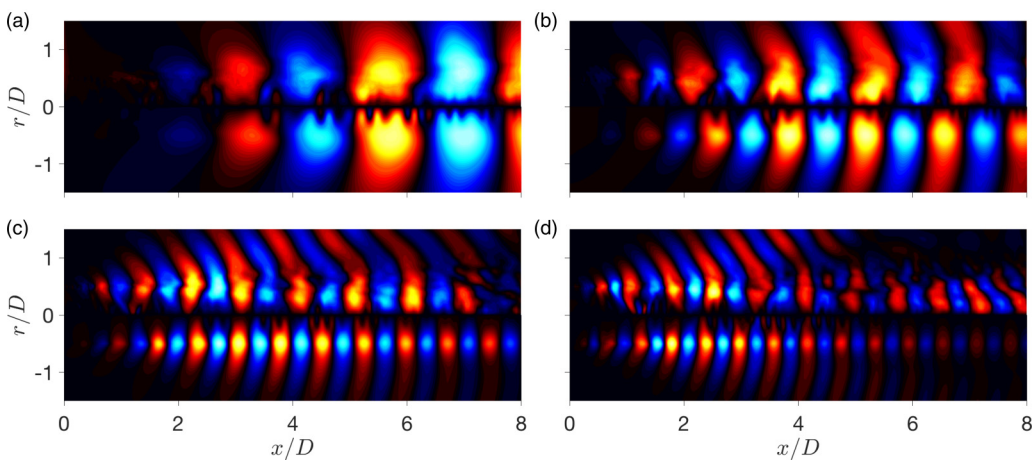


FIG. 17. Comparison between leading SPOD modes from LES (top) and the flow structure predicted by PFE (bottom) using  $N = 4$  and several frequencies. Real part of the modes are shown for  $St = 0.19$  (a),  $0.4$  (b),  $0.74$  (c), and  $0.91$  (d). Only positive wave numbers are allowed in the SPOD, and the PFE reconstruction is performed using nonnegative components.

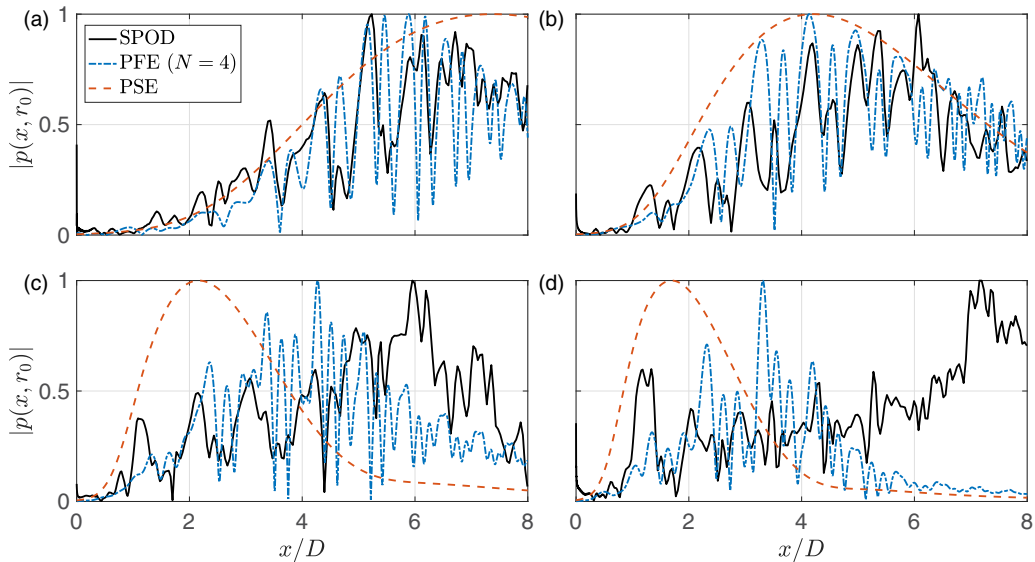


FIG. 18. Absolute value of leading SPOD modes from LES compared to PFE ( $N = 4$ ) and PSE results for several frequencies. Magnitude of the modes extracted at  $r/D = 0.1$  for  $St = 0.19$  (a),  $0.4$  (b),  $0.74$  (c), and  $0.91$  (d). Only positive wave numbers are allowed in the SPOD, and the PFE reconstruction is performed using nonnegative components. All curves are normalized by their maximum.

filtered SPOD and nonnegative components of PFE. Compared to Figs. 11 and 12, the modulation of the SPOD modes seems consistently weaker for all frequencies, suggesting that the negative wave numbers are responsible for a stronger modulation effect than their positive counterparts, or that the presence of upstream waves is responsible for a substantial part of the observed modulation; at this point, it is impossible to separate these two effects. PFE modes are also less strongly modulated, and most of the observed oscillations are concentrated around the centerline in Fig. 11. The filter is shown to improve the overall agreement, which can also be seen in the radial structure and wavelengths of the wave packet in Fig. 17. The amplitude of the modulations are compared for  $r/D = 0.1$  in Fig. 18. Without the presence of the negative component of the modulation, the agreement between PFE and filtered SPOD improves, especially at the early stations of the jet (see Fig. 13, particularly the position of the peaks). Due to the presence of higher harmonics, the model is able to predict the position of both medium and large peaks, as smaller oscillations are associated with higher-order modulation components.

These results show that, despite its limitations, PFE can be used as a prediction tool for shock-containing jets. At this point, it is worth highlighting all the modeling steps taken to obtain these results: (1) a consideration of a mean flow that is not exactly what is observed in the LES; (2) the approximation of a train of shock cells (which are related to steep variations of fluid properties) as a ductlike mode predicted using a linear stability model; (3) the truncation of the solution to a limited number of harmonics (only the modulation associated with the leading shock-cell mode is computed); (4) the absence of turbulent forcing/viscosity in the flow, with coherent structures being predicted using a linear model; and (5) the application of the model to a case where it is not supposed to perform ideally. Despite all these steps, many features of the modulated wave packets are captured by this severely simplified model. As in PSE, the PFE formulation does not need any input from experiments, except for an equivalent ideally expanded flow (which can be modeled as in the present analysis). This makes the method suitable for the prediction of coherent structures where no time-resolved data are available, as is the case in the vast majority of shock-containing jets.

## V. CONCLUSIONS

In this work, we propose a formulation to predict modulated coherent structures in shock-containing jets based on the method developed by Ran *et al.* [41]. First, the shock-cell structure for a given flow condition is approximated using the parabolized stability equations (PSE) applied to a modeled ideally expanded jet. This solution is then used to define a shock-containing mean flow, around which the Navier-Stokes equations are linearized. By means of a Floquet ansatz, a set of equations is obtained, in which the positive and negative components of the modulation (related to the local shock-cell wave number) are considered in the response vector. The final equations have the same shape as in PSE and are solved in the same fashion, rendering the name parabolized Floquet equations (PFE) [41]. We show that the formulation constitutes the quasiperiodic counterpart of PSE, therefore bearing several similarities. It is also shown that PFE is more restrictive than PSE due to the repetition of the modes in the eigenspectrum of the linear operators (as also noted by Nogueira *et al.* [30]), potentially requiring substantially larger spatial steps for the march, depending on the flow conditions and the frequency of analysis.

The method was applied to two cases. The first considered an underexpanded jet at low supersonic Mach number, modeled as a canonical slowly diverging flow. The solution procedure was shown in detail for two frequencies, which included a description of the process of obtaining the initial solution to be marched downstream. The modulation characteristics of the resulting axisymmetric wave packet were explored, and the initial results suggested that the modulation can be very sensitive to the different modes supported by the flow at a given frequency. Overall, some characteristics of the flow structures obtained using PFE were similar to results in the literature, providing a first validation of the method. After that, the same methodology was applied to predict the most energetic (nonscreeching) helical structures from an LES of an overexpanded jet. For that, a slightly more complex mean flow model was chosen to better match the LES data. Using such a model, PSE was able to predict the overall behavior of the shock-cell structure, especially its leading wave number and its variation in spacing further downstream. Using this solution, PFE modes were computed and compared to pressure SPOD modes for azimuthal wave number  $m = 1$ . Qualitative agreement was obtained, especially closer to the centerline of the jet, suggesting that the method is able to capture the underlying physical mechanisms for the generation of these structures: the extraction of energy from the mean flow by the Kelvin-Helmholtz mode, and a redistribution of energy to modulation wave numbers due to the interaction with the shock-cell structure, as predicted by Tam and Tanna [35]. The model outperforms the classic PSE method, providing a good first approximation of the wave packets supported by the flow, despite its several limitations. No experimental input is needed for the predictions of wave-packet shapes, but a representative ideally expanded mean flow must be provided. While zero-frequency PSE is used to predict the overall behavior of the shock-cell structure, a decomposition of an experimentally obtained shock-containing mean flow following the same structure as in the present case could also be used as input in the analysis. The model also provides an alternative to global methods: as a spatial marching method, PFE demands less memory and produces results much faster than global resolvent analysis, especially considering the high Reynolds numbers of these flows. At this point, it is unclear how nonlinear PSE would perform compared to linear PFE for shock-containing jets, especially considering that no such formulation is available in the literature for this case. However, as the present PFE formulation does not focus on the interaction between modes at different frequencies, nonlinear PSE may not be the appropriate tool to study these flows. Furthermore, as highlighted by Ran *et al.* [41], PFE avoids the complexity induced by the computation of the nonlinear terms in the physical space, making it a simpler approach to these problems.

The present framework opens avenues for modeling and control of shock-containing jets. The modulated wave-packet model can be used for BBSAN source modeling [40] and similar installed jet noise [65] predictions for generic flow conditions. It can also be used as input for real-time flow predictions that could be applied in designing control strategies for noise reduction [66]. Finally, the general Floquet formulation used to obtain the PFE could also be used to build other high-fidelity

prediction models, such as the one-way Navier-Stokes equations [59,67]. The explicit filtering of upstream waves in the one-way method has the potential to solve most of the issues of the present formulation, allowing for a clear separation between upstream waves and negative wave-number modulation.

### ACKNOWLEDGMENTS

This work was supported by the Australian Research Council through the Discovery Project scheme: DP190102220. We thank G. Brès for generously providing the overexpanded jet LES database used in the present manuscript and K. Sasaki for providing a first version of his PSE code. The authors report no conflict of interest.

### APPENDIX A: LINEAR OPERATORS FOR THE PARABOLIZED FLOQUET EQUATIONS

We can exemplify how the PFE solution is obtained by working with the linearized continuity equation. Neglecting the mean radial velocity, this equation can be written as

$$-i\omega v + \bar{u} \frac{\partial v}{\partial x} + u \frac{\partial \bar{v}}{\partial x} + v \frac{\partial \bar{v}}{\partial r} - v \frac{\partial \bar{u}}{\partial x} - \bar{v} \left( \frac{\partial u}{\partial x} + \frac{\partial v}{\partial r} + \frac{v}{r} + \frac{im}{r} w \right) = 0. \quad (\text{A1})$$

Inserting (13) (using  $N = 1$ ) into (A1) and ignoring all the terms in  $\Gamma_s^{\pm 2}$ , we can write the continuity equation as a function of the different modulation components. In other formulations, such as nonlinear PSE (or even SPLSA [30]), the explicit dependence on a single wave number  $\alpha_s$  allows us to write three different equations from the equation above: one dependent on  $\Gamma_s^0 = 1$ , one on  $\Gamma_s$  and another one on  $\Gamma_s^* = \Gamma_s^{-1}$ . The same argument is used here, by considering the collection to be performed at each streamwise station (since the shock-cell wave number is slowly varying, this approximation should still be representative of the phenomenon). Using that assumption, we can separate the evolution of disturbances related to the different powers of  $\Gamma_s$ . Namely, for  $\Gamma_s^0$  we can write

$$\begin{aligned} & \left[ -i\omega \hat{v}_0 + \bar{u}_0 \left( \frac{\partial \hat{v}_0}{\partial x} + i\alpha \hat{v}_0 \right) + \hat{u}_0 \frac{\partial \bar{v}_0}{\partial x} + \hat{v}_0 \frac{\partial \bar{v}_0}{\partial r} \right. \\ & \quad \left. - \hat{v}_0 \frac{\partial \bar{u}_0}{\partial x} - \bar{v}_0 \left( \frac{\partial \hat{u}_0}{\partial x} + i\alpha \hat{u}_0 \right) - \bar{v}_0 \left( \frac{\partial}{\partial r} + \frac{1}{r} \right) \hat{v}_0 - \bar{v}_0 \frac{im}{r} \hat{w}_0 \right] \\ & + \left[ u_s^* \left( \frac{\partial \hat{v}_{+1}}{\partial x} + i(\alpha + \alpha_s) \hat{v}_{+1} \right) + \hat{u}_{+1} \left( \frac{\partial v_s^*}{\partial x} - i\alpha_s v_s^* \right) + \hat{v}_{+1} \frac{\partial v_s^*}{\partial r} \right. \\ & \quad \left. - \hat{v}_{+1} \left( \frac{\partial u_s^*}{\partial x} - i\alpha_s u_s^* \right) - v_s^* \left( \frac{\partial \hat{u}_{+1}}{\partial x} + i(\alpha + \alpha_s) \hat{u}_{+1} \right) - v_s^* \left( \frac{\partial}{\partial r} + \frac{1}{r} \right) \hat{v}_{+1} - v_s^* \frac{im}{r} \hat{w}_{+1} \right] \\ & + \left[ u_s \left( \frac{\partial \hat{v}_{-1}}{\partial x} + i(\alpha - \alpha_s) \hat{v}_{-1} \right) + \hat{u}_{-1} \left( \frac{\partial v_s}{\partial x} + i\alpha_s v_s \right) + \hat{v}_{-1} \frac{\partial v_s}{\partial r} - \hat{v}_{-1} \left( \frac{\partial u_s}{\partial x} + i\alpha_s u_s \right) \right. \\ & \quad \left. - v_s \left( \frac{\partial \hat{u}_{-1}}{\partial x} + i(\alpha - \alpha_s) \hat{u}_{-1} \right) - v_s \left( \frac{\partial}{\partial r} + \frac{1}{r} \right) \hat{v}_{-1} - v_s \frac{im}{r} \hat{w}_{-1} \right] = 0, \quad (\text{A2}) \end{aligned}$$

for  $\Gamma_s$

$$\begin{aligned} & \left[ -i\omega \hat{v}_{+1} + \bar{u}_0 \left( \frac{\partial \hat{v}_{+1}}{\partial x} + i(\alpha + \alpha_s) \hat{v}_{+1} \right) + \hat{u}_{+1} \frac{\partial \bar{v}_0}{\partial x} + \hat{v}_{+1} \frac{\partial \bar{v}_0}{\partial r} \right. \\ & \quad \left. - \hat{v}_{+1} \frac{\partial \bar{u}_0}{\partial x} - \bar{v}_0 \left( \frac{\partial \hat{u}_{+1}}{\partial x} + i(\alpha + \alpha_s) \hat{u}_{+1} \right) - \bar{v}_0 \left( \frac{\partial}{\partial r} + \frac{1}{r} \right) \hat{v}_{+1} - \bar{v}_0 \frac{im}{r} \hat{w}_{+1} \right] \end{aligned}$$

$$\begin{aligned}
 & + \left[ u_s \left( \frac{\partial \hat{v}_0}{\partial x} + i\alpha \hat{v}_0 \right) + \hat{u}_0 \left( \frac{\partial v_s}{\partial x} + i\alpha_s v_s \right) + \hat{v}_0 \frac{\partial v_s}{\partial r} \right. \\
 & \left. - \hat{v}_0 \left( \frac{\partial u_s}{\partial x} + i\alpha_s u_s \right) - v_s \left( \frac{\partial \hat{u}_0}{\partial x} + i\alpha \hat{u}_0 \right) - v_s \left( \frac{\partial}{\partial r} + \frac{1}{r} \right) \hat{v}_0 - v_s \frac{im}{r} \hat{w}_0 \right] = 0, \quad (\text{A3})
 \end{aligned}$$

and equivalently for  $\Gamma_s^*$ .

The symmetry of the equations above becomes apparent by comparing the terms inside square brackets with (A1), which helps us to build the equivalent system. By applying the same process to the Navier-Stokes and energy equations, we obtain

$$\begin{aligned}
 & -i\omega \begin{bmatrix} \hat{\mathbf{q}}_{-1} \\ \hat{\mathbf{q}}_0 \\ \hat{\mathbf{q}}_{+1} \end{bmatrix} + \begin{bmatrix} \mathbf{L}_0 & \mathbf{L}_s^* & O \\ \mathbf{L}_s & \mathbf{L}_0 & \mathbf{L}_s^* \\ O & \mathbf{L}_s & \mathbf{L}_0 \end{bmatrix} \begin{bmatrix} \hat{\mathbf{q}}_{-1} \\ \hat{\mathbf{q}}_0 \\ \hat{\mathbf{q}}_{+1} \end{bmatrix} + \begin{bmatrix} \mathbf{B}_0 & \mathbf{B}_s^* & O \\ \mathbf{B}_s & \mathbf{B}_0 & \mathbf{B}_s^* \\ O & \mathbf{B}_s & \mathbf{B}_0 \end{bmatrix} \frac{\partial}{\partial x} \begin{bmatrix} \hat{\mathbf{q}}_{-1} \\ \hat{\mathbf{q}}_0 \\ \hat{\mathbf{q}}_{+1} \end{bmatrix} \\
 & + i\alpha \begin{bmatrix} \mathbf{B}_0 & \mathbf{B}_s^* & O \\ \mathbf{B}_s & \mathbf{B}_0 & \mathbf{B}_s^* \\ O & \mathbf{B}_s & \mathbf{B}_0 \end{bmatrix} \begin{bmatrix} \hat{\mathbf{q}}_{-1} \\ \hat{\mathbf{q}}_0 \\ \hat{\mathbf{q}}_{+1} \end{bmatrix} + i\alpha_s \begin{bmatrix} -\mathbf{B}_0 & O & O \\ -\mathbf{B}_s & O & \mathbf{B}_s^* \\ O & O & \mathbf{B}_0 \end{bmatrix} \begin{bmatrix} \hat{\mathbf{q}}_{-1} \\ \hat{\mathbf{q}}_0 \\ \hat{\mathbf{q}}_{+1} \end{bmatrix} = 0, \quad (\text{A4})
 \end{aligned}$$

which is the explicit form of system (14) for  $N = 1$ , with

$$\mathbf{L}_t = \begin{bmatrix} \mathbf{L}_0 & \mathbf{L}_s^* & O \\ \mathbf{L}_s & \mathbf{L}_0 & \mathbf{L}_s^* \\ O & \mathbf{L}_s & \mathbf{L}_0 \end{bmatrix}, \quad \mathbf{B}_t = \begin{bmatrix} \mathbf{B}_0 & \mathbf{B}_s^* & O \\ \mathbf{B}_s & \mathbf{B}_0 & \mathbf{B}_s^* \\ O & \mathbf{B}_s & \mathbf{B}_0 \end{bmatrix}, \quad \mathbf{B}_{st} = \begin{bmatrix} -\mathbf{B}_0 & O & O \\ -\mathbf{B}_s & O & \mathbf{B}_s^* \\ O & O & \mathbf{B}_0 \end{bmatrix}. \quad (\text{A5})$$

The operators  $\mathbf{L}_0$ ,  $\mathbf{L}_s$ ,  $\mathbf{L}_s^*$ ,  $\mathbf{B}_0$ ,  $\mathbf{B}_s$ , and  $\mathbf{B}_s^*$  are given by

$$\begin{aligned}
 \mathbf{L}_0 = & \begin{bmatrix} -\partial_x \bar{u}_0 & \partial_x \bar{v}_0 & \partial_r \bar{v}_0 - \bar{v}_0 (D_r + \frac{1}{r}) & -im \frac{\bar{v}_0}{r} & 0 \\ \partial_x \bar{p}_0 & \partial_x \bar{u}_0 & \partial_r \bar{u}_0 & 0 & 0 \\ \partial_r \bar{p}_0 & 0 & 0 & 0 & \bar{v}_0 D_r \\ 0 & 0 & 0 & 0 & im \frac{\bar{v}_0}{r} \\ 0 & \partial_x \bar{p}_0 & \partial_r \bar{p}_0 + \gamma \bar{p}_0 D_r + \gamma \frac{\bar{p}_0}{r} & im \gamma \frac{\bar{p}_0}{r} & \gamma \partial_x \bar{u}_0 \end{bmatrix} \\
 & - \frac{1}{\text{Re}} \begin{bmatrix} 0 & 0 & 0 & 0 & 0 & 0 \\ \partial_r^2 \bar{u}_0 + \frac{\partial_r \bar{u}_0}{r} & \bar{v}_0 \Delta & 0 & 0 & 0 & 0 \\ 0 & 0 & \bar{v}_0 (\Delta - \frac{1}{r^2}) & -\frac{2im \bar{v}_0}{r^2} & 0 & 0 \\ 0 & 0 & \frac{2im \bar{v}_0}{r^2} & \bar{v}_0 (\Delta - \frac{1}{r^2}) & 0 & 0 \\ \frac{\gamma}{\text{Pr}} (\bar{p}_0 \Delta + \partial_r^2 \bar{p}_0 + \frac{\partial_r \bar{p}_0}{r}) & 0 & 0 & 0 & 0 & \frac{\gamma}{\text{Pr}} (\bar{v}_0 \Delta + \partial_r^2 \bar{v}_0 + \frac{\partial_r \bar{v}_0}{r}) \end{bmatrix}, \quad (\text{A6})
 \end{aligned}$$

$$\begin{aligned}
 \mathbf{L}_s = & \begin{bmatrix} -(\partial_x u_s + i\alpha_s u_s) & \partial_x v_s + i\alpha_s v_s & \partial_r v_s - v_s (D_r + \frac{1}{r}) & -im \frac{v_s}{r} & 0 \\ \partial_x p_s + i\alpha_s p_s & \partial_x u_s + i\alpha_s u_s & \partial_r u_s & 0 & 0 \\ \partial_r p_s & 0 & 0 & 0 & v_s D_r \\ 0 & 0 & 0 & 0 & im \frac{v_s}{r} \\ 0 & \partial_x p_s + i\alpha_s p_s & \partial_r p_s + \gamma p_s D_r + \gamma \frac{p_s}{r} & im \gamma \frac{p_s}{r} & \gamma (\partial_x u_s + i\alpha_s u_s) \end{bmatrix} \\
 & - \frac{1}{\text{Re}} \begin{bmatrix} 0 & 0 & 0 & 0 & 0 \\ \partial_r^2 \bar{u}_s + \frac{\partial_r \bar{u}_s}{r} & \bar{v}_s \Delta & 0 & 0 & 0 \\ 0 & 0 & \bar{v}_s (\Delta - \frac{1}{r^2}) & -\frac{2im \bar{v}_s}{r^2} & 0 \\ 0 & 0 & \frac{2im \bar{v}_s}{r^2} & \bar{v}_s (\Delta - \frac{1}{r^2}) & 0 \\ \frac{\gamma}{\text{Pr}} (\bar{p}_s \Delta + \partial_r^2 \bar{p}_s + \frac{\partial_r \bar{p}_s}{r}) & 0 & 0 & 0 & \frac{\gamma}{\text{Pr}} (\bar{v}_s \Delta + \partial_r^2 \bar{v}_s + \frac{\partial_r \bar{v}_s}{r}) \end{bmatrix}
 \end{aligned}$$

$$-\frac{1}{\text{Re}} \begin{bmatrix} 0 & 0 & 0 & 0 & 0 \\ -\bar{u}_s \alpha_s^2 + 2i\alpha_s \partial_x \bar{u}_s + i\bar{u}_s \partial_x \alpha_s & 0 & 0 & 0 & 0 \\ 0 & 0 & 0 & 0 & 0 \\ 0 & 0 & 0 & 0 & 0 \\ \frac{\gamma}{\text{Pr}} (-\bar{p}_s \alpha_s^2 + 2i\alpha_s \partial_x \bar{p}_s + i\bar{p}_s \partial_x \alpha_s) & 0 & 0 & 0 & \frac{\gamma}{\text{Pr}} (-\bar{v}_s \alpha_s^2 + 2i\alpha_s \partial_x \bar{v}_s + i\bar{v}_s \partial_x \alpha_s) \end{bmatrix}, \quad (\text{A7})$$

$$\mathbf{L}_{\mathbf{s}^*} = \begin{bmatrix} -(\partial_x u_s^* - i\alpha_s u_s^*) & \partial_x v_s^* - i\alpha_s v_s^* & \partial_r v_s^* - v_s^* (D_r + \frac{1}{r}) & -im \frac{v_s^*}{r} & 0 \\ \partial_x p_s^* - i\alpha_s p_s^* & \partial_x u_s^* - i\alpha_s u_s^* & \partial_r u_s^* & 0 & 0 \\ \partial_r p_s^* & 0 & 0 & 0 & v_s^* D_r \\ 0 & 0 & 0 & 0 & im \frac{v_s^*}{r} \\ 0 & \partial_x p_s^* - i\alpha_s p_s^* & \partial_r p_s^* + \gamma p_s^* D_r + \gamma \frac{p_s^*}{r} & im \gamma \frac{p_s^*}{r} & \gamma (\partial_x u_s^* - i\alpha_s u_s^*) \end{bmatrix}$$

$$-\frac{1}{\text{Re}} \begin{bmatrix} 0 & 0 & 0 & 0 & 0 \\ \partial_r^2 \bar{u}_s^* + \frac{\partial_r \bar{u}_s^*}{r} & \bar{v}_s^* \Delta & 0 & 0 & 0 \\ 0 & 0 & \bar{v}_s^* (\Delta - \frac{1}{r^2}) & -\frac{2im\bar{v}_s^*}{r^2} & 0 \\ 0 & 0 & \frac{2im\bar{v}_s^*}{r^2} & \bar{v}_s^* (\Delta - \frac{1}{r^2}) & 0 \\ \frac{\gamma}{\text{Pr}} (\bar{p}_s^* \Delta + \partial_r^2 \bar{p}_s^* + \frac{\partial_r \bar{p}_s^*}{r}) & 0 & 0 & 0 & \frac{\gamma}{\text{Pr}} (\bar{v}_s^* \Delta + \partial_r^2 \bar{v}_s^* + \frac{\partial_r \bar{v}_s^*}{r}) \end{bmatrix}$$

$$-\frac{1}{\text{Re}} \begin{bmatrix} 0 & 0 & 0 & 0 & 0 \\ -\bar{u}_s^* \alpha_s^2 - 2i\alpha_s \partial_x \bar{u}_s^* - i\bar{u}_s^* \partial_x \alpha_s & 0 & 0 & 0 & 0 \\ 0 & 0 & 0 & 0 & 0 \\ 0 & 0 & 0 & 0 & 0 \\ \frac{\gamma}{\text{Pr}} (-\bar{p}_s^* \alpha_s^2 - 2i\alpha_s \partial_x \bar{p}_s^* - i\bar{p}_s^* \partial_x \alpha_s) & 0 & 0 & 0 & \frac{\gamma}{\text{Pr}} (-\bar{v}_s^* \alpha_s^2 - 2i\alpha_s \partial_x \bar{v}_s^* - i\bar{v}_s^* \partial_x \alpha_s) \end{bmatrix}, \quad (\text{A8})$$

$$\mathbf{B}_0 = \begin{bmatrix} \bar{u}_0 & -\bar{v}_0 & 0 & 0 & 0 \\ 0 & \bar{u}_0 & 0 & 0 & \bar{v}_0 \\ 0 & 0 & \bar{u}_0 & 0 & 0 \\ 0 & 0 & 0 & \bar{u}_0 & 0 \\ 0 & \gamma \bar{p}_0 & 0 & 0 & \bar{u}_0 \end{bmatrix}, \quad (\text{A9})$$

$$\mathbf{B}_{\mathbf{s}} = \begin{bmatrix} u_s & -v_s & 0 & 0 & 0 \\ 0 & u_s & 0 & 0 & v_s \\ 0 & 0 & u_s & 0 & 0 \\ 0 & 0 & 0 & u_s & 0 \\ 0 & \gamma p_s & 0 & 0 & u_s \end{bmatrix}, \quad (\text{A10})$$

$$\mathbf{B}_{\mathbf{s}^*} = \begin{bmatrix} u_s^* & -v_s^* & 0 & 0 & 0 \\ 0 & u_s^* & 0 & 0 & v_s^* \\ 0 & 0 & u_s^* & 0 & 0 \\ 0 & 0 & 0 & u_s^* & 0 \\ 0 & \gamma p_s^* & 0 & 0 & u_s^* \end{bmatrix}, \quad (\text{A11})$$

where  $D_r$  is the radial differential operator,  $\partial_{x,r}$  indicates streamwise and radial derivatives of the mean flow quantities (including the shock-cell components) and  $\gamma$  is the specific heat ratio. One should also note that, for the PSE case, the operators  $\mathbf{L}$  and  $\mathbf{B}$  reduce to  $\mathbf{L}_0$  and  $\mathbf{B}_0$ . The operator  $\Delta$  is given by

$$\Delta = D_r^2 + \frac{1}{r} D_r - \frac{m^2}{r^2}. \quad (\text{A12})$$

As usual in PSE formulations, the second streamwise derivatives of flow disturbances were ignored. The second streamwise derivatives of the ideally expanded mean flow and of the slowly

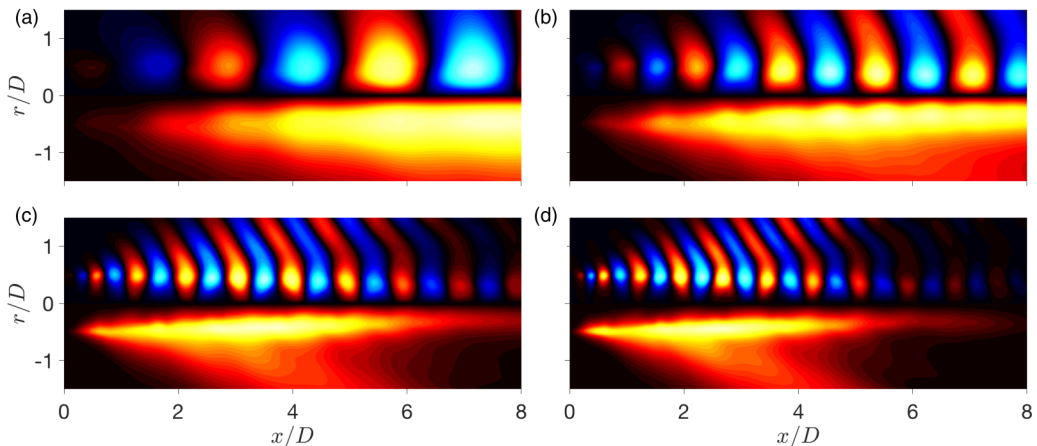


FIG. 19. Pressure fields predicted by PSE using the LES mean flow. Both real part (top) and absolute value (bottom) are shown for  $St = 0.19$  (a),  $0.4$  (b),  $0.74$  (c), and  $0.91$  (d).

varying part of the shock-cell structure were also neglected, but all the other terms were retained, including the terms associated with the second derivative of the oscillatory part of the mean flow. The tridiagonal structure of the operators above remain the same for the  $N > 1$  cases; specifically, the operator  $\mathbf{B}_{st}$  for arbitrary  $N$  is given by

$$\mathbf{B}_{st} = \begin{bmatrix} -N\mathbf{B}_0 & (-N+1)\mathbf{B}_{s^*} & O & \dots & O & O & O \\ -N\mathbf{B}_s & (-N+1)\mathbf{B}_0 & (-N+2)\mathbf{B}_{s^*} & \dots & O & O & O \\ O & (-N+1)\mathbf{B}_s & (-N+2)\mathbf{B}_0 & \dots & O & O & O \\ \vdots & & & \ddots & & & \vdots \\ O & O & O & \dots & (N-2)\mathbf{B}_0 & (N-1)\mathbf{B}_s & O \\ O & O & O & \dots & (N-2)\mathbf{B}_{s^*} & (N-1)\mathbf{B}_0 & N\mathbf{B}_s \\ O & O & O & \dots & O & (N-1)\mathbf{B}_{s^*} & N\mathbf{B}_0 \end{bmatrix}. \quad (\text{A13})$$

## APPENDIX B: PSE RESULTS FOR SHOCK-CONTAINING MEAN FLOW

Application of PSE requires a slowly varying mean flow and that the resulting functions  $\hat{\mathbf{q}}$  and  $\alpha$  are also slowly varying. While these conditions can be satisfied in perfectly expanded jets, shock-containing jet are usually considered to break these hypotheses *a priori*. The fast streamwise variation of these flows prohibits the coarse spatial marching of PSE, and results are more subject to numerical instability due to the sharp radial variations of the mean velocity caused by the shocks. Here we ignore these assumptions and evaluate the PSE solution when the shock-containing mean flow shown in Fig. 10(a) is given as input. Note that the streamwise variation of the mean flow is not small, especially due to the presence of the shock-cell structure and of the small Mach disk close to the nozzle. Sample pressure fields for the same frequencies studied in this work are shown in Fig. 19. Interestingly, some modulation is observed in these wave packets, mainly due to small local variations in the wave number  $\alpha$ . Still, since PSE only supports a single peak wave number (and small streamwise variations of it), this modulation is not comparable with the SPOD results, which are severely affected by the shock cells. Overall, these results bear more resemblance to the shock-free PSE, with smooth variations of the resulting modes in the streamwise direction.

That said, Fig. 19 shows that PSE captures the near-field sound generated by the wave packets at these frequencies. As no quasiperiodicity is considered in this formulation, the distance between the KH and upstream modes in the eigenspectrum for higher frequencies is large, allowing for smaller spatial steps and, as a result, for a better representation of the sound generation mechanism.

- 
- [1] E. Mollo-Christensen, Jet noise and shear flow instability seen from an experimenter's viewpoint (Similarity laws for jet noise and shear flow instability as suggested by experiments), *J. Appl. Mech.* **34**, 1 (1967).
  - [2] S. C. Crow and F. H. Champagne, Orderly structure in jet turbulence, *J. Fluid Mech.* **48**, 547 (1971).
  - [3] A. V. G. Cavalieri, P. Jordan, T. Colonius, and Y. Gervais, Axisymmetric superdirectivity in subsonic jets, *J. Fluid Mech.* **704**, 388 (2012).
  - [4] P. Jordan and T. Colonius, Wave packets and turbulent jet noise, *Annu. Rev. Fluid Mech.* **45**, 173(2013).
  - [5] A. V. G. Cavalieri, P. Jordan, and L. Lesshafft, Wave-packet models for jet dynamics and sound radiation, *Appl. Mech. Rev.* **71**, 020802 (2019).
  - [6] A. Michalke, On the inviscid instability of the hyperbolic tangent velocity profile, *J. Fluid Mech.* **19**, 543 (1964).
  - [7] A. Michalke, On spatially growing disturbances in an inviscid shear layer, *J. Fluid Mech.* **23**, 521 (1965).
  - [8] G. L. Brown and A. Roshko, On density effects and large structure in turbulent mixing layers, *J. Fluid Mech.* **64**, 775 (1974).
  - [9] A. Michalke, *Instabilität eines kompressiblen runden Freistrahls unter Berücksichtigung des Einflusses der Strahlgrenzschichtdicke (instability of a compressible circular jet considering the influence of the thickness of the jet boundary layer)*, DEUTSCHE FORSCHUNGS-UND VERSUCHSANSTALT FUER LUFT-UND RAUMFAHRT EV BERLIN (West Germany, 1971), <https://apps.dtic.mil/sti/citations/AD0739069>.
  - [10] G. E. Mattingly and C. C. Chang, Unstable waves on an axisymmetric jet column, *J. Fluid Mech.* **65**, 541 (1974).
  - [11] D. G. Crighton and M. Gaster, Stability of slowly diverging jet flow, *J. Fluid Mech.* **77**, 397 (1976).
  - [12] F. Bertolotti and T. Herbert, Analysis of the linear stability of compressible boundary layers using the PSE, *Theor. Comput. Fluid Dyn.* **3**, 117 (1991).
  - [13] T. Herbert, Parabolized stability equations, Spec. Course Progr. Transition Modell. (AGARD) **793**, 1 (1994).
  - [14] T. Herbert, Parabolized stability equations, *Annu. Rev. Fluid Mech.* **29**, 245 (1997).
  - [15] K. Gudmundsson and T. Colonius, Instability wave models for the near-field fluctuations of turbulent jets, *J. Fluid Mech.* **689**, 97 (2011).
  - [16] A. Towne, O. T. Schmidt, and T. Colonius, Spectral proper orthogonal decomposition and its relationship to dynamic mode decomposition and resolvent analysis, *J. Fluid Mech.* **847**, 821 (2018).
  - [17] K. Sasaki, A. V. G. Cavalieri, P. Jordan, O. T. Schmidt, T. Colonius, and G. A. Brès, High-frequency wavepackets in turbulent jets, *J. Fluid Mech.* **830**, R2 (2017).
  - [18] A. Sinha, D. Rodríguez, G. A. Brès, and T. Colonius, Wavepacket models for supersonic jet noise, *J. Fluid Mech.* **742**, 71 (2014).
  - [19] A. Sinha, K. Gudmundsson, H. Xia, and T. Colonius, Parabolized stability analysis of jets from serrated nozzles, *J. Fluid Mech.* **789**, 36 (2016).
  - [20] B. J. McKeon and A. S. Sharma, A critical-layer framework for turbulent pipe flow, *J. Fluid Mech.* **658**, 336 (2010).
  - [21] O. T. Schmidt, A. Towne, G. Rigas, T. Colonius, and G. A. Brès, Spectral analysis of jet turbulence, *J. Fluid Mech.* **855**, 953 (2018).
  - [22] L. Lesshafft, O. Semeraro, V. Jaunet, A. V. G. Cavalieri, and P. Jordan, Resolvent-based modeling of coherent wave packets in a turbulent jet, *Phys. Rev. Fluids* **4**, 063901 (2019).

- [23] E. Pickering, G. Rigas, P. A. S. Nogueira, A. V. G. Cavalieri, O. T. Schmidt, and T. Colonius, Lift-up, Kelvin–Helmholtz and Orr mechanisms in turbulent jets, *J. Fluid Mech.* **896**, A2 (2020).
- [24] P. A. S. Nogueira, A. V. G. Cavalieri, P. Jordan, and V. Jaunet, Large-scale streaky structures in turbulent jets, *J. Fluid Mech.* **873**, 211 (2019).
- [25] L. I. Abreu, A. V. G. Cavalieri, P. Schlatter, R. Vinuesa, and D. S. Henningson, Spectral proper orthogonal decomposition and resolvent analysis of near-wall coherent structures in turbulent pipe flows, *J. Fluid Mech.* **900**, A11 (2020).
- [26] P. A. S. Nogueira, P. Morra, E. Martini, A. V. G. Cavalieri, and D. S. Henningson, Forcing statistics in resolvent analysis: Application in minimal turbulent Couette flow, *J. Fluid Mech.* **908**, A32 (2021).
- [27] P. Morra, P. A. S. Nogueira, A. V. G. Cavalieri, and D. S. Henningson, The colour of forcing statistics in resolvent analyses of turbulent channel flows, *J. Fluid Mech.* **907**, A24 (2021).
- [28] G. Raman, Advances in understanding supersonic jet screech: Review and perspective, *Prog. Aerosp. Sci.* **34**, 45 (1998).
- [29] D. Edgington-Mitchell, Aeroacoustic resonance and self-excitation in screeching and impinging supersonic jets—A review, *Int. J. Aeroacoust.* **18**, 118 (2019).
- [30] P. A. Nogueira, P. Jordan, V. Jaunet, A. V. Cavalieri, A. Towne, and D. Edgington-Mitchell, Absolute instability in shock-containing jets, *J. Fluid Mech.* **930**, A10 (2022).
- [31] S. Beneddine, C. Mettot, and D. Sipp, Global stability analysis of underexpanded screeching jets, *Eur. J. Mech. B* **49**, 392 (2015).
- [32] D. Edgington-Mitchell, T. Wang, P. Nogueira, O. Schmidt, V. Jaunet, D. Duke, P. Jordan, and A. Towne, Waves in screeching jets, *J. Fluid Mech.* **913**, A7 (2021).
- [33] F. P. Bertolotti, T. Herbert, and P. R. Spalart, Linear and nonlinear stability of the Blasius boundary layer, *J. Fluid Mech.* **242**, 441 (1992).
- [34] M. Harper-Bourne and M. J. Fisher, The noise from shock waves in supersonic jets, *Agard Cp-131* **11**, 1 (1974).
- [35] C. K. W. Tam and H. K. Tanna, Shock associated noise of supersonic jets from convergent-divergent nozzles, *J. Sound Vib.* **81**, 337 (1982).
- [36] C. Tam, Stochastic model theory of broadband shock associated noise from supersonic jets, *J. Sound Vib.* **116**, 265 (1987).
- [37] P. J. Morris and S. A. E. Miller, Prediction of broadband shock-associated noise using Reynolds-averaged Navier-Stokes computational fluid dynamics, *AIAA J.* **48**, 2931 (2010).
- [38] D. Tan, D. Honnery, A. Kalyan, V. Gryazev, S. Karabasov, and D. Edgington-Mitchell, Equivalent shock-associated noise source reconstruction of screeching underexpanded unheated round jets, *AIAA J.* **57**, 1200 (2019).
- [39] P. K. Ray and S. K. Lele, Sound generated by instability wave/shock-cell interaction in supersonic jets, *J. Fluid Mech.* **587**, 173 (2007).
- [40] M. H. Wong, P. Jordan, I. A. Maia, A. V. Cavalieri, R. Kirby, T. C. Fava, and D. Edgington-Mitchell, Wavepacket modelling of broadband shock-associated noise in supersonic jets, *J. Fluid Mech.* **918**, A9 (2021).
- [41] W. Ran, A. Zare, M. J. Philipp Hack, and M. R. Jovanović, Modeling mode interactions in boundary layer flows via the parabolized Floquet equations, *Phys. Rev. Fluids* **4**, 023901 (2019).
- [42] A. S. Towne, Advancements in jet turbulence and noise modeling: Accurate one-way solutions and empirical evaluation of the nonlinear forcing of wavepackets, Ph.D. thesis, California Institute of Technology, 2016.
- [43] C. K. W. Tam, J. A. Jackson, and J. M. Seiner, A multiple-scales model of the shock-cell structure of imperfectly expanded supersonic jets, *J. Fluid Mech.* **153**, 123 (1985).
- [44] T. Herbert, Secondary instability of boundary layers, *Annu. Rev. Fluid Mech.* **20**, 487 (1988).
- [45] A. Towne, G. Rigas, and T. Colonius, A critical assessment of the parabolized stability equations, *Theor. Comput. Fluid Dyn.* **33**, 359 (2019).
- [46] S. Beneddine, D. Sipp, A. Arnault, J. Dandois, and L. Lesshafft, Conditions for validity of mean flow stability analysis, *J. Fluid Mech.* **798**, 485 (2016).

- [47] P. A. S. Nogueira, V. Jaunet, M. Mancinelli, P. Jordan, and D. Edgington-Mitchell, Closure mechanism of the A1 and A2 modes in jet screech, *J. Fluid Mech.* **936**, A10 (2022).
- [48] P. Huerre and P. A. Monkewitz, Absolute and convective instabilities in free shear layers, *J. Fluid Mech.* **159**, 151 (1985).
- [49] F. Li and M. R. Malik, Mathematical nature of parabolized stability equations, in *Laminar-Turbulent Transition*, edited by R. Kobayashi (Springer, Berlin, 1995), pp. 205–212.
- [50] P. Andersson, D. Henningson, and A. Hanifi, On a stabilization procedure for the parabolic stability equations, *J. Eng. Math.* **33**, 311 (1998).
- [51] C. K. W. Tam and F. Q. Hu, On the three families of instability waves of high-speed jets, *J. Fluid Mech.* **201**, 447 (1989).
- [52] A. Towne, A. V. G. Cavalieri, P. Jordan, T. Colonius, O. Schmidt, V. Jaunet, and G. A. Brès, Acoustic resonance in the potential core of subsonic jets, *J. Fluid Mech.* **825**, 1113 (2017).
- [53] J. A. Weideman and S. C. Reddy, A MATLAB differentiation matrix suite, *ACM Trans. Math. Softw. (TOMS)* **26**, 465 (2000).
- [54] L. Lesshafft and P. Huerre, Linear impulse response in hot round jets, *Phys. Fluids* **19**, 024102 (2007).
- [55] M.-R. Choi and S. K. Lele, Prediction of shock-cell structure using parabolized stability equations, in *AIAA Paper 2001-0744 presented at the 39th Aerospace Sciences Meeting and Exhibit, 8–11 January* (Reno, NV, USA, 2001), p. 744.
- [56] D. C. Pack, A note on Prandtl’s formula for the wave-length of a supersonic gas jet, *Q. J. Mech. Appl. Math.* **3**, 173 (1950).
- [57] D. Rodríguez, M. R. Jotkar, and E. M. Gennaro, Wavepacket models for subsonic twin jets using 3D parabolized stability equations, *C. R. Mec.* **346**, 890 (2018).
- [58] D. Edgington-Mitchell, V. Jaunet, P. Jordan, A. Towne, J. Soria, and D. Honnery, Upstream-travelling acoustic jet modes as a closure mechanism for screech, *J. Fluid Mech.* **855**, R1 (2018).
- [59] A. Towne and T. Colonius, One-way spatial integration of hyperbolic equations, *J. Comput. Phys.* **300**, 844 (2015).
- [60] G. A. Brès, F. E. Ham, J. W. Nichols, and S. K. Lele, Unstructured large-eddy simulations of supersonic jets, *AIAA J.* **55**, 1164 (2017).
- [61] G. A. Brès, P. Jordan, V. Jaunet, M. Le Rallic, A. V. G. Cavalieri, A. Towne, S. K. Lele, T. Colonius, and O. T. Schmidt, Importance of the nozzle-exit boundary-layer state in subsonic turbulent jets, *J. Fluid Mech.* **851**, 83 (2018).
- [62] A. V. G. Cavalieri, D. Rodríguez, P. Jordan, T. Colonius, and Y. Gervais, Wavepackets in the velocity field of turbulent jets, *J. Fluid Mech.* **730**, 559 (2013).
- [63] N. D. Sandham and A. M. Salgado, Nonlinear interaction model of subsonic jet noise, *Philos. Trans. R. Soc. A* **366**, 2745 (2008).
- [64] M. J. Lighthill, On sound generated aerodynamically. I. General theory, *Proc. R. Soc. London, Ser. A* **211**, 564 (1952).
- [65] P. A. Nogueira, A. V. Cavalieri, and P. Jordan, A model problem for sound radiation by an installed jet, *J. Sound Vib.* **391**, 95 (2017).
- [66] K. Sasaki, S. Piantanida, A. V. G. Cavalieri, and P. Jordan, Real-time modelling of wavepackets in turbulent jets, *J. Fluid Mech.* **821**, 458 (2017).
- [67] M. Zhu and A. Towne, Recursive one-way Navier Stokes equations with PSE-like cost, [arXiv:2111.10040](https://arxiv.org/abs/2111.10040).